Title
Cryostat design for the computed tomodensitometer (CTD)

Author
Faulkner, Kenneth G.

Publication Date
1988

Peer reviewed|Thesis/dissertation

CRYOSTAT DESIGN FOR THE COMPUTED TOMODENSITOMETER (CTD)

by

KENNETH G. FAULKNER

THESIS

Submitted in partial satisfaction of the requirements for the degree of

MASTER OF SCIENCE

in

BIOENGINEERING

in the

GRADUATE DIVISION

of the

UNIVERSITY OF CALIFORNIA

San Francisco

[redacted]

Date

University Librarian

Degree Conferred: . . . . . .

Preface

This thesis is submitted in partial fulfillment of the requirements for the Master of Science Degree in Bioengineering through the University of California Joint Bioengineering Graduate Program at the Berkeley and San Francisco campuses. The project was funded in part by JPL Subcontract 956084.

The work presented here is only a small part of an extended study being conducted at the University of California, San Francisco, designed to investigate bone mineral losses due to disease, disuse, and extended space flight. Of the many people involved in this research, I would like to thank Dr. Chris Cann and Dr. Brian Rutt for first introducing me to the technique of bone mineral determination using computed tomography, as well as the staff of Imatron and the UCSF Physics Research Lab, where most of this work was done. I would especially like to thank Dr. Bruce Hasegawa of the Physics Research Lab for his guidance, patience and trust during my research. Besides being a wonderful mentor and advisor during the past year, he has also become a great friend.

Title: Cryostat Design for the Computed Tomodensitometer (CTD)

Author: Kenneth G. Faulkner

Joint Graduate Program in Bioengineering

University of California, San Francisco

Abstract

Physicists at the University of California, San Francisco have designed a Computed Tomodensitometer (CTD) for the precise determination of bone mineral content *in vivo* . Tomographic images displaying bone density and distribution using dual energy techniques are obtained using a samarium filtered x-ray beam. Detection is performed with nineteen high-purity germanium crystals, each one segemented into 24 elements for a total of 456 detection channels. The germanium crystals are cooled using a liquid nitrogen cryostat that unlike conventional cryostat assemblies is rotatable and designed to be mounted on a gantry for obtaining tomographic images. The temperature of the crystals is kept within a few degrees of the boiling point of liquid nitrogen (77K) to reduce thermally generated noise. The heat loss rate of the system is designed to be 2 watts so that the liquid nitrogen tank need only be filled once a week. The electrical connections to the detector crystals are made using vacuum feedthroughs and specially designed flex circuits. A smaller prototype cryostat that holds three crystals has been in operation for several months and has successfully maintained the crystals at 83K while consuming only one liter of liquid nitrogen per day.

Contents

Tables

Figures and Illustrations

Chapter 1: Introduction

I. Background

Bone is composed of three tissue types: cortical bone, trabecular bone, and marrow. The cortical or compact bone is denser and forms an outside layer encasing the inner or trabecular bone. Inside the trabecular matrix of the adult vertebrae, ribs, sternum, skull and proximal epiphyses of the femur and humerus is found the red marrow which acts as the site of red blood cell manufacture.

The trabecular bone forms lattice-like patterns in the bone core which usually follow the direction and magnitude of applied stresses on the bone. If the stress is removed for extended periods of time as in prolonged bed rest or space flight, some mineral loss is usually exhibited by the trabecular areas, while cortical losses may be minimal. In selected bones, such as the vertebrae, a fatty material called yellow marrow is also found inside the bone matrix. Unlike cortical and trabecular tissues, this material has essentially no mineral content and serves primarily as a food reserve.

The bone mineral content, which is composed predominantly of calcium carbonate and calcium phosphate, is a direct reflection of the structural integrity of the bone. Several studies have demonstrated the positive correlation between bone strength and measured bone mineral content (1-6). Two types of bone deficiency are defined clinically. The term osteomalacia is used to describe deficiency in mineralized bone

while osteoporosis describes a lack of both the mineral and the collagenous matrix. A number of patient conditions may lead to bone mineral loss including immobilization, normal aging, renal disease, and genetic metabolic disorders (7). Early detection of abnormal bone mineral losses could be used to identify patients at an increased risk to fracture.

Bone demineralization during space flight has been observed by both American and Soviet biologists. Studies performed on Gemini crew members showed marked mineral losses as a direct consequence of weightlessness (8,9). Similarly, Soviet biologists reported significant bone mineral losses in the members of the Soyuz and Saylut space station crews and the amount of mineral lost increased with the duration of weightlessness (10). The most severe losses were reported in Skylab crew members, with as much as 10% loss from the predominantly trabecular calcaneus (heel bone) during a three month mission (11).

Bone cell and calcium metabolic changes in spaceflight have been documented to occur within the first three to ten days of weightlessness (12). These changes may cause small but irreversible decrement in bone mass which will only be measurable with repeated exposure to weightlessness or with instruments of very high precision. While a bone loss of one to two percent after a one week flight may not cause a significantly increased risk of fracture, a one to two percent loss is equivalent to the bone change which would normally be experienced in one year. Thus repeated short term flights could lead to the premature bone mineral loss.

NASA has expended a considerable amount of effort to investigate the effect of weightlessness on the musculoskeletal system. Of particular interest are non-invasive methods to measure and monitor bone mineral levels of current and potential flight personnel. Several methods are currently used to quantitatively assess bone mineral content in cases of prolonged immobilization and osteoporosis. Among the most widely used are radiogrammetry and single photon absorptiometry which are limited to measuring cortical bone in the appendicular skeleton. Measures of integral (cortical plus trabecular) bone in the axial skeleton are currently being made using neutron activation analysis and dual-photon absorptiometry. Included in Appendix A is a brief description of each of these methods along with their advantages and limitations. More recently, x-ray computed tomography has proven to be an effective method for measuring trabecular bone at both central and peripheral sites.

II. Bone Mineral Determination Using Computed Tomography

Due to the insensitivity of cortical and integral bone mineral measurements (see Appendix A), a few techniques have been developed for the measurement of purely trabecular bone. At the present, the only method in routine clinical use is computed tomography, also known as CT (13-39).

The usefulness of CT for bone mineral assessment lies in its ability to provide a cross-sectional image, either centrally or peripherally. Thus, a major advantage of computed tomography over other bone mineral techniques is the capability to spatially separate cortical and

trabecular bone. Trabecular bone has a turnover rate of up to eight times that of cortical bone due to a high surface to volume ratio and other physiological factors (13). This high turnover rate makes trabecular bone a highly sensitive measurement site for early detection of bone mineral loss.

Quantitative computed tomography (QCT) has proven effective in measuring trabecular mineral content in the spine (14,16-22,24-29, 38), in the radius (13,23,24,34-37) and in the tibia (39). The vertebral body is especially well suited for bone mineral studies due to its relatively large trabecular bone content. QCT techniques have been used at the University of California, San Francisco to study vertebral mineral changes in osteoporosis and other metabolic bone diseases. In these studies, the values for bone mineral content are obtained using a General Electric CT/T 8800 or CT/T 9800 rotary fan-beam scanner. A crescent shaped normalization phantom is placed on the patient table and is scanned along with the patient to calibrate against scanner drift. The phantom contains solutions of K_2HPO_4 (roughly equivalent to bone mineral), ethanol (fat equivalent), glycerol, and water (soft tissue equivalent) (17). The CT numbers derived from the calibration phantom scanned simultaneously with the patient are used to calculate the mineral equivalent for each vertebrae.

The entire scan takes between 10 and 15 minutes to complete and the total radiation dose to the upper abdomen is 100 to 200 mrem (20). Currently, QCT is being used at several research centers and at a variety of clinics for spinal trabecular mineral determination using a wide variety of commercial scanners.

III. The Proposed Computed Tomodensitometer (CTD)

The small changes in bone mineral content expected in short term space flight require instrumentation which can measure the most metabolically active bone (trabecular bone in the spine) with a precision error of 0.5 percent or less and with a radiation dose low enough (roughly 10 to 100 mrem) to allow serial measurements over short term. Current techniques fall short in both of these areas. Theoretically, changes in bone density of as little as 0.2 percent should be detectable using a low-dose whole-body CT scanner, yet only about 2 percent precision is currently being realized (12). This failure to attain theoretically maximum precision is caused largely by instabilities in the various components used in commercial scanners, most notably the x-ray source and the detectors.

Bone mineral measurement accuracy is known to be degraded by variable fat or marrow content (24). Because of the finite resolution of CT scanners, the reconstructed image elements usually contain a mixture of different materials such as bone, marrow and fat. Each of these different materials has its own attenuation properties, so that the average attenuation of an image element depends on the type and amount of materials present.

If there are only two materials and a single photon energy, a single scan can determine their relative amounts because their absolute densities and attenuations are known. This is a consequence of the attenuation equation

$$I = I_o \exp[-(\mu_1 d_1 + \mu_2 d_2)]$$

where

I = transmitted radiation intensity

I_o = incident radiation intensity

μ_j = linear attenuation coefficient of material j

d_j = thickness of material j

The total thickness of the material, D, is subject to the constraint that

$$D = d_1 + d_2$$

However, if there are three materials, the quantity of each cannot be determined uniquely. To do this, some other physical property of one or more of the materials must be exploited. In CT, this can be done by acquiring images at two photon energies, changing the relative contributions of the photoelectric and Compton attenuation of the x-ray beam. This adds a third equation to the previous set of only two:

$$\text{At energy } E_1\text{: } I_1 = (I_1)_o \exp[-(\mu_{1,1}d_1 + \mu_{1,2}d_2 + \mu_{1,3}d_3)]$$

$$\text{At energy } E_2\text{: } I_2 = (I_2)_o \exp[-(\mu_{2,1}d_1 + \mu_{2,2}d_2 + \mu_{2,3}d_3)]$$

where

I_j = transmitted radiation intensity for energy j

$(I_j)_o$ = incident radiation intensity for energy j

d_j = thickness of material j

$\mu_{i,j}$ = gamma ray linear attenuation coefficient for material j at energy i

The relative amounts of each of the materials can be determined under the constraint that

$$D = d_1 + d_2 + d_3$$

This technique is termed dual-energy CT and has been used to successfully separate components in liver (40), brain (41) and bone (24,42). Optimal choice of the two effective energies depends on the material being studied and the minimum required noise level in the image; however, the basic premise is that one should use as wide an energy separation as possible to achieve good contrast without delivering excessive dose to the patient.

In 1979, physicists at the University of California at San Francisco (UCSF) proposed the development of a low-dose whole-body scanner which would reach the limits of computed tomographic bone mineral determination (43). They planned to achieve this goal by using dual-energy computed tomography together with highly stable filtered x-ray sources and photon counting detectors. The proposed device came to be known as the Computed Tomodensitometer (CTD), since it would basically be a specialized computed tomographic scanner optimized for bone mineral measurements rather than high resolution images. The originally proposed CTD consisted of two gadolinium-153 sources along with a low-power x-ray tube mounted on a stationary 360 degree ring of high-purity germanium detectors (figure 1). Gadolinium-153 is the isotope typically employed in dual photon absorptiometry and is a good source of 42 and 100 keV photons. These energies turn out to be optimal for dual energy bone mineral measurements in the spine (12).

It was soon determined, however, that the gadolinium-153 spectrum could be well approximated using a samarium filtered x-ray

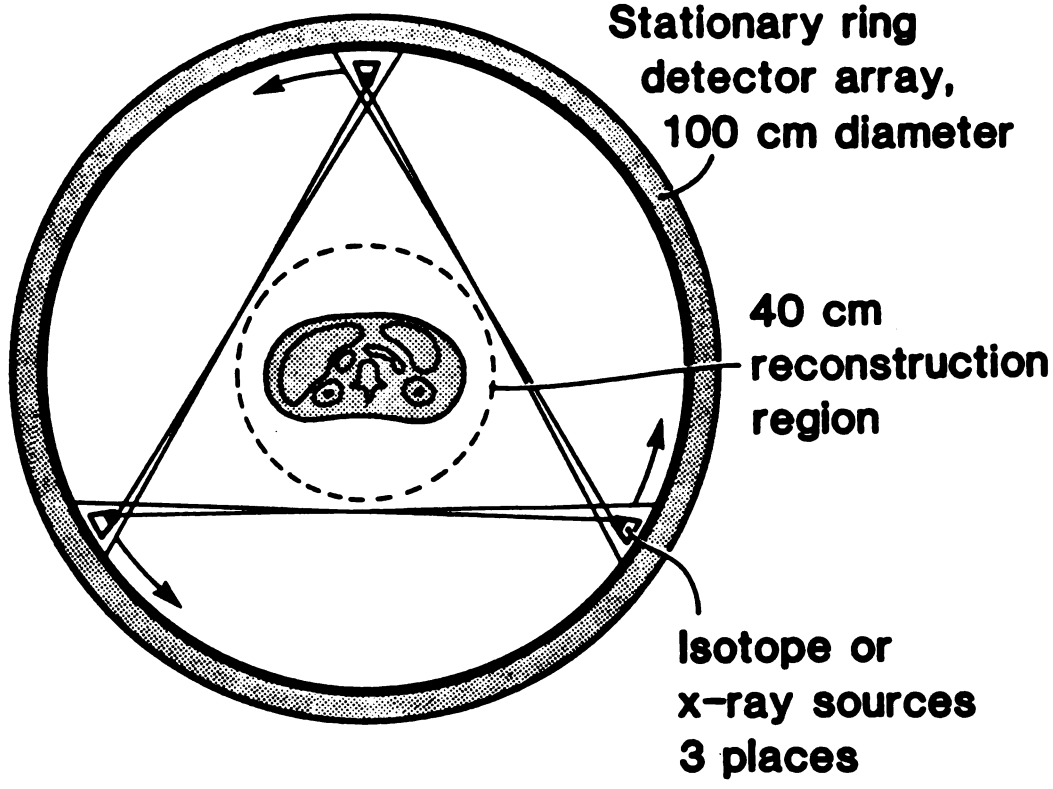

Figure 1: Originally proposed CTD configuration showing the 360^0 ring of detectors and 3 separate x-ray sources rotating inside the stationary ring.

beam. Samarium has a K-edge at 43 keV (representing the binding energy of the K-shell electrons) so that a 0.5 mm to 1.0 mm thick sheet placed over the x-ray tube portal shapes the spectrum into two components with peaks approximating those of the gadolinium isotope (figure 2).

A highly stable x-ray tube with a samarium filter provides an economical dual-energy x-ray source which simulates the gamma ray spectrum from gadolinium-153 but which neither decays nor requires periodic replacement, as does the gadolinium-153 isotope source with a half-life of only 241 days. Thus the decision was made to eliminate the two isotope sources and use only a single low-power x-ray tube.

It also became readily apparent that a 360 degree detector ring of germanium crystals would be economically infeasible. The cost of the crystals as well as the electronics required for data collection prompted the change from a fourth generation geometry (rotating source with stationary detectors) to that of third generation (rotating source and detectors). Thus only a partial arc of crystals would be needed to detect the entire x-ray beam, but with the disadvantage that the detectors and preamplification electronics would have to rotate with the x-ray source.

The first CTD to be sent to NASA will be constructed using the gantry from an Technicare 2010 commercial scanner which has been updated and modified using the CTD technology. The commercial x-ray tube and conventional scintillation detectors are to be replaced with a highly stable x-ray tube and a specially designed detector array described in chapter 2. The dimensions of the current CTD design are presented in figure 3 and were chosen to match the gantry

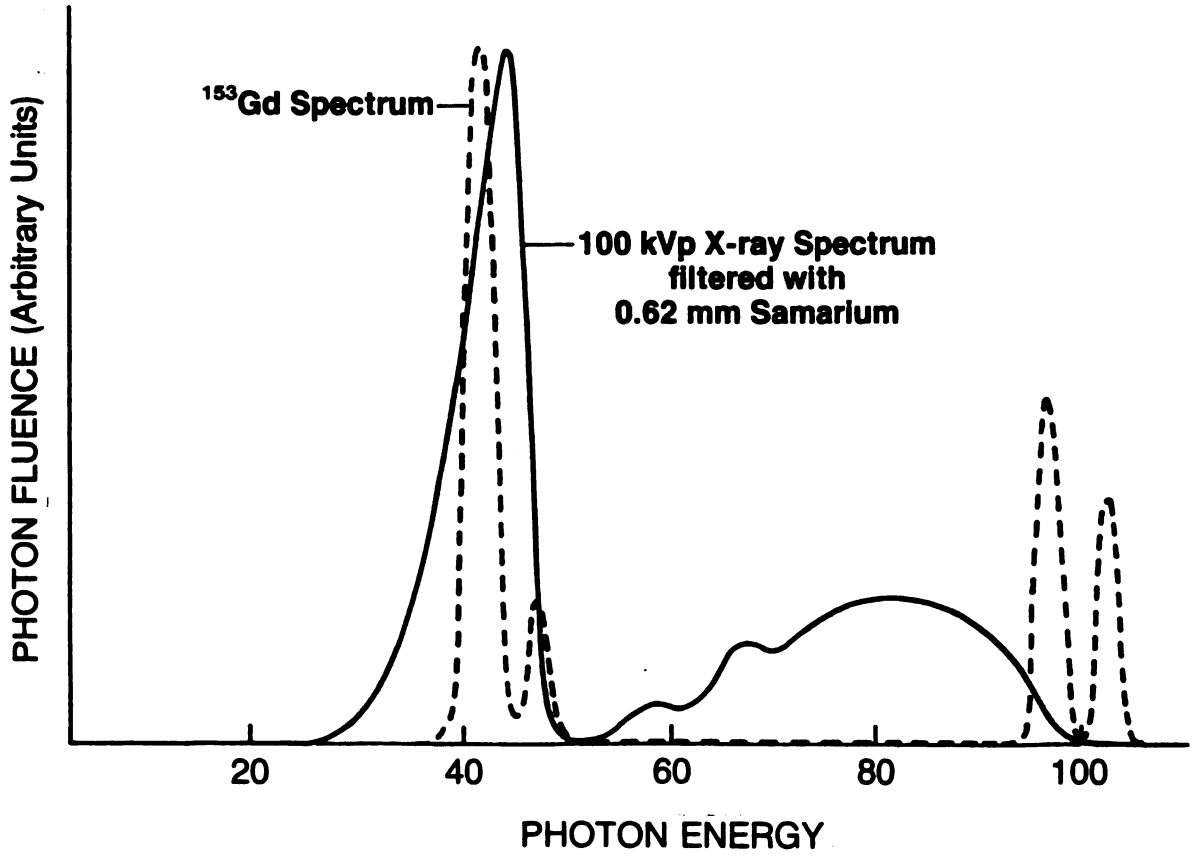

Figure 2: 100 kVp x-ray spectrum (solid line) filtered with 0.62 mm of samarium shown together with the spectrum of Gd-153 (dotted line). Both spectra were obtained using the same high-purity germanium detector.

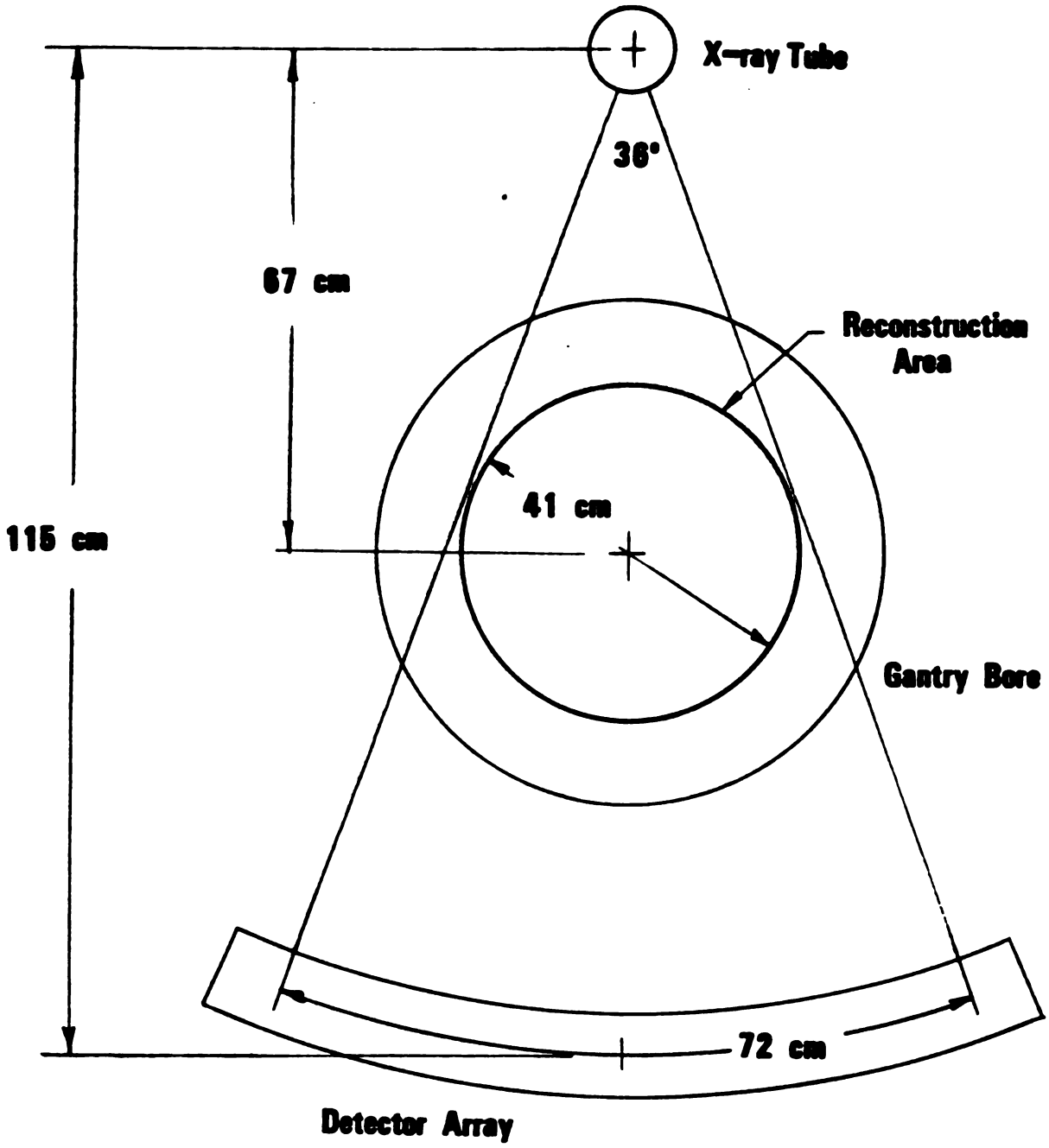

Figure 3: CTD geometry according to the dimensions of the Technicare 2010 gantry. Using these dimensions, a 41 cm reconstruction diameter is possible.

configuration of the Technicare 2010 scanner. In the future, a specialized gantry may be designed which will be much smaller and lighter weight and readily adaptable to operation in a space station. A schematic diagram which outlines the entire NASA CTD system is presented in figure 4.

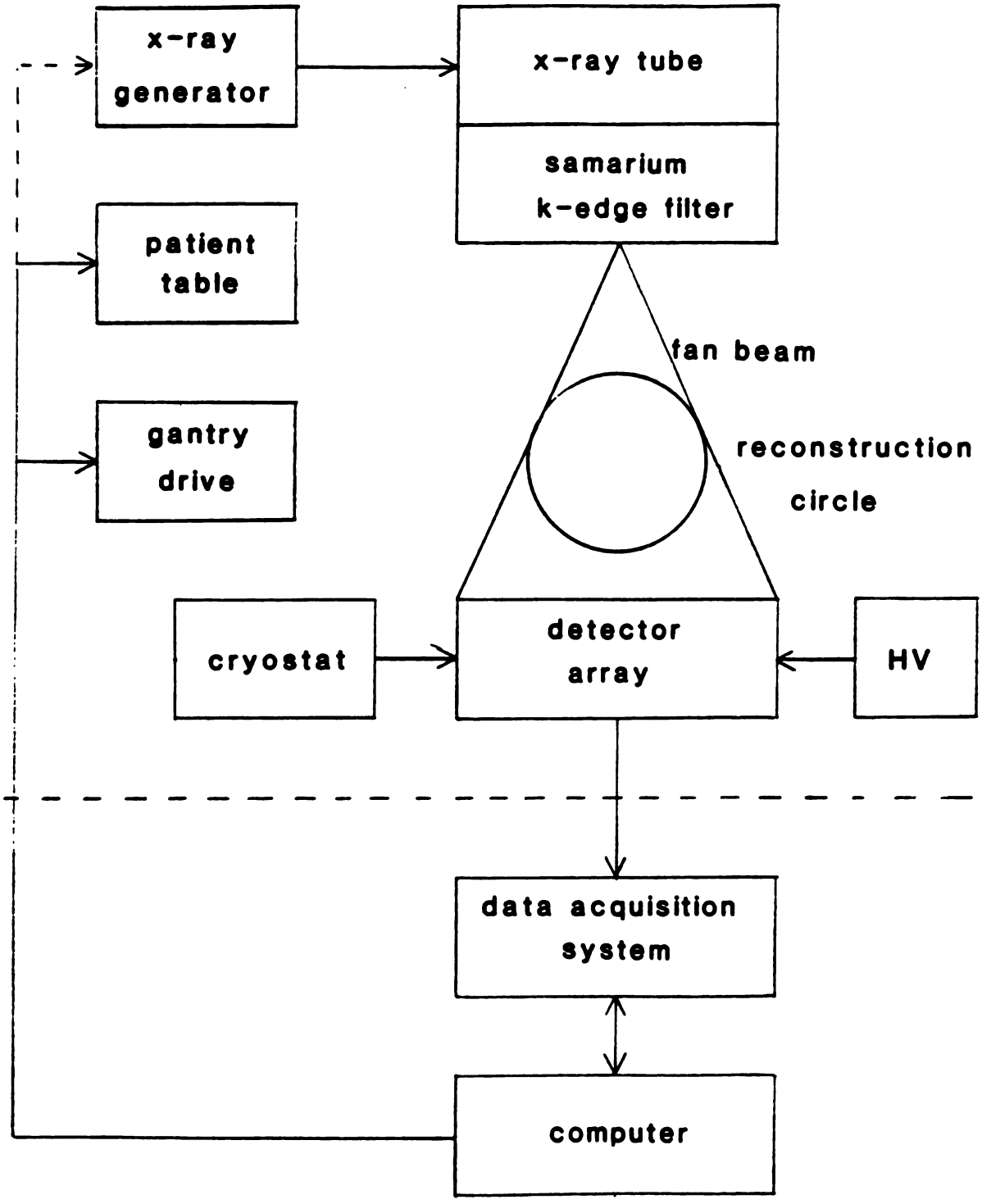

Figure 4: Schematic showing the main components of the CTD. A Sun microcomputer is used to control the x-ray generator, patient table, gantry drive and data acquisition system. This computer also reconstructs the bone density images for display and analysis. The fan beam from an x-ray tube is filtered through samarium and then detected using an array of 19 germanium crystals sectioned into a total of 456 elements. These crystals are reverse biased using a high-voltage (HV) power supply and cooled in the CTD cryostat.

Chapter 2: The CTD Detector Array

I. High-Purity Germanium Detectors

The majority of commercial scanners employ either gas-ionization or scintillation detectors operating in what is known as integrating mode. These detectors monitor the total energy deposited by the interaction of many x-ray photons with the detector material and produce a current signal in proportion to the amount of energy collected. However, at low x-ray intensities these detectors are susceptible to electronic fluctuations and substantial dark currents, both of which degrade signal to noise performance. In these situations, detectors capable of counting individual photons, that is, operating in counting mode, are preferred. The precision of these detectors is limited by the counting statistics only, and, in principal, is not affected by electronic noise.

The best available material for this purpose is high-purity germanium because of its good stopping power for diagnostic x-rays (in the range of 40 to 140 keV) and extremely fast response times (approximately 50 ns for a 5 mm thick detector). High-purity germanium can be manufactured in crystal arrays composed of individual detector elements spaced by only a few millimeters.

Germanium crystals are classed as semiconductor detectors or more generally, solid state detectors. The detection process in a semiconductor is analogous to that of the ionization of a gas. The

incident radiation lifts an electron from the highest filled band (the valence band) to the conduction band; the energy difference between the two bands is called the band gap.

In semiconductors the band gap is of the order of 1 eV (small enough for thermal excitation to cause some conduction), whereas in insulators it is several times larger, on the order of 5 to 10 eV. When an electron is lifted into the conduction band, thus acquiring a high mobility, a positive hole is created in the valence band which can also 'move', not by bodily movement of the ion through the crystal but by successive electron exchanges between neighboring lattice sites. The energy W required to produce an electron-hole pair always exceeds the band gap since some energy goes into coupling electrons to lattice vibrations. This is similar to the situation in gases where the energy required for ion-pair formation always exceeds the ionization potential because some energy is used in the excitation and dissociation process. For germanium, W = 2.96 eV for gamma rays and electrons at 77K, where for silicon, another commonly used semiconductor detector, W = 3.76 eV. The corresponding values of the band gap are 0.67 and 1.12 eV, respectively.

The low value of the band gap makes it necessary to operate germanium detectors at cryogenic temperatures to avoid excessive thermal excitations. Despite this disadvantage, germanium crystals are preferred to silicon for gamma ray detection because the relatively high atomic number and density gives them good sensitivity to gamma rays. Table 1 gives a comparison of the properties of intrinsic (i.e high purity) silicon and germanium.

Table 1. Properties of Intrinsic Silicon and Germanium

	Si	Ge
Atomic number	14	32
Atomic weight	28.09	72.60
Stable isotope mass numbers	28,29,30	70,72,73,74,76
Density (300K); g cm^{-3}	2.33	5.33
Atoms cm^{-3}	4.96×10^{22}	4.41×10^{22}
Dielectric constant	12	16
Band gap (300K); eV	1.115	0.665
Band gap (0K); eV	1.165	0.746
Intrinsic carrier density (300K); cm^{-3}	1.5×10^{10}	2.4×10^{13}
Intrinsic resistivity (300K); Ωcm	2.3×10^{5}	47
Electron mobility (300K); cm^2/ V-s	1350	3900
Hole mobility (300K); cm^2/ V-s	480	1900
Electron mobility (77K); cm^2/ V-s	2.1×10^{4}	3.6×10^{4}
Hole mobility (77K); cm^2/ V-s	1.1×10^{4}	4.2×10^{4}
Energy per electron-hole pair (300K); eV	3.62	
Energy per electron-hole pair (77K); eV	3.76	2.96

From G. Bertolini and A. Coche, Eds., *Semiconductor Detectors*, Elsevier-North Holland, Amsterdam (1968)

When a gamma ray passes through a semiconductor, the overall effect is the production of many electron-hole pairs along the track of the ray. The number of electron-hole pairs produced is proportional to the energy of the incident gamma ray. If an electric field is applied to the semiconductor material, these electrons and holes will migrate. The motion will be a combination of random thermal velocity and a net drift velocity parallel to the direction of the applied field. These electrons can be collected, yielding a signal pulse which will be proportional to the number of electrons produced and hence the energy of the gamma ray.

For a 60 keV gamma ray, approximately 20,000 electron-hole pairs (also called carriers) are formed. Assuming Poisson statistics, the statistical counting error for this case is $(20{,}000)^{0.5}/20{,}000 \times 100\%$ or 0.7%. For gas-filled and scintillating detectors, the same 60 keV gamma ray produces only one-tenth this number of carriers because of the proportionately higher energy required per electron-hole pair production. Thus the statistical fluctuation in the number of carriers per pulse becomes $(2000)^{0.5}/2000 \times 100\%$ or 2.2% which represents a much larger fraction of the total. For these reasons, the energy resolution of high-purity germanium is substantially better than either gas-filled or scintillation detectors.

Figure 5 shows gadolinium-153 spectra obtained at the UCSF Physics Research Laboratory using a single element of a segmented germanium detector compared to a conventional sodium iodide scintillation detector. The sodium iodide detector failed to distinguish between the two energies present in both the high and low peaks of

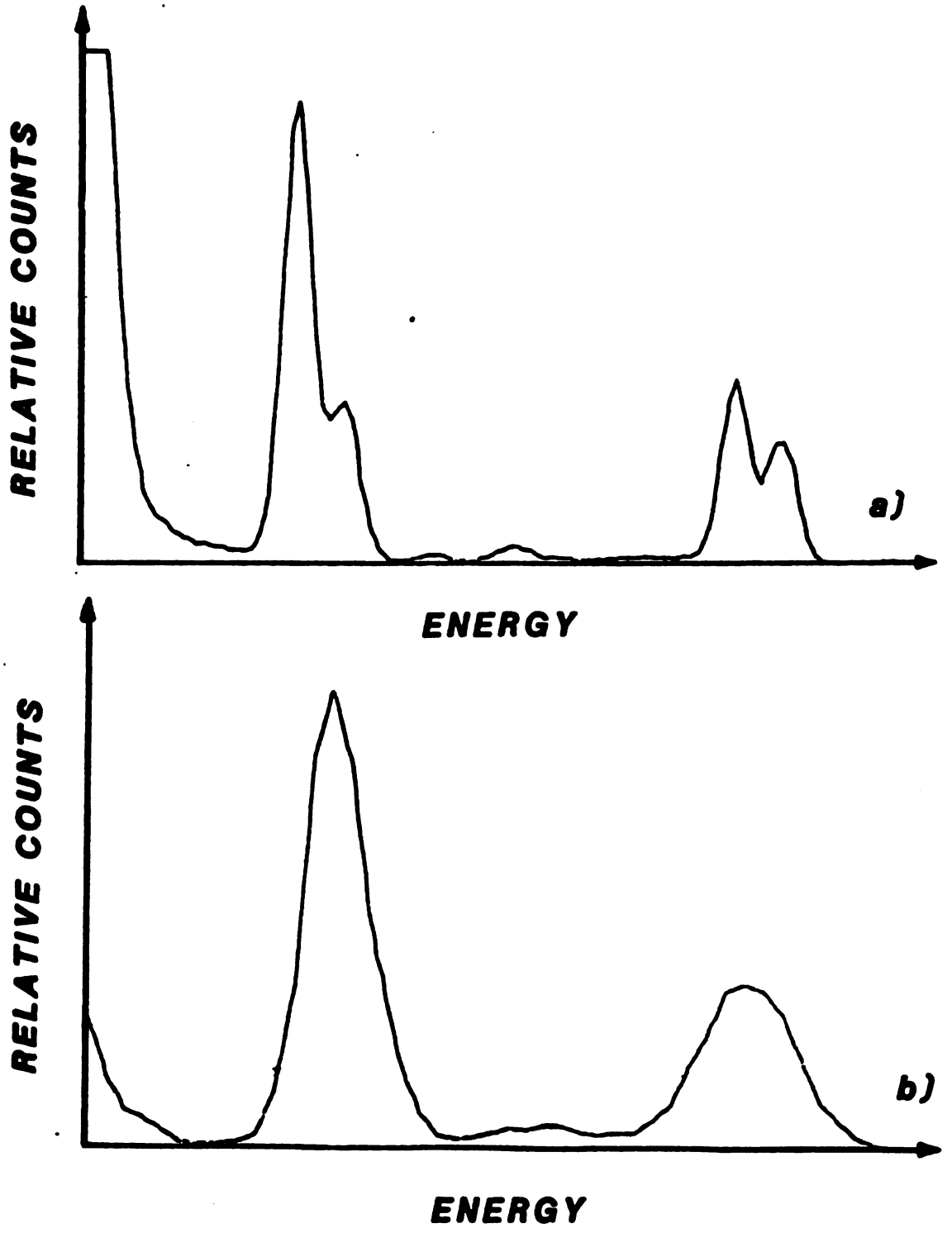

Figure 5a: Gd-153 spectrum using one element of the high-purity germanium detector showing double peaks for the low energy (at 41 and 47 keV) and for the high energy (at 97 and 103 keV). Full-width-half-maximum energy resolution is approximately 5 keV.

Figure 5b: Gd-153 spectrum obtained with a sodium iodide scintillation detector

the gadolinium-153 spectrum. The germanium detector, however, easily resolved these discrete energy levels.

In order to efficiently collect the liberated electrons to produce a signal pulse, the germanium crystal must be reversed biased with an electric field. At low values of electric field intensity, the drift velocity of the electrons and holes is roughly proportional to the applied field. At higher electric field values, the drift velocity increases more slowly until eventually a saturation velocity is reached. For germanium, the saturation velocity is of the order of 10^7 cm/s, which means for a typical 0.5 cm thick crystal, the collection time will be around 50 nanoseconds. Germanium detectors are therefore among the fastest responding of all radiation detector types capable of count rates of 10^3 to 10^6 counts per second with minimal dead time. In practice the counting rates will only be limited by the electronics of preamplification and not by the efficiency of the detector or the intensity of the x-ray beam.

II. Detector Crystal Design

The commercial use of semiconductor detectors has been limited, since gas-filled and scintillation detectors are adequate for clinical requirements. The technology of the CTD, however, requires the use of germanium detectors in order to reach the theoretical limits of CT precision. The current design calls for crystals having 48 mm by 10 mm detection area and a 6 mm absorption thickness. Each crystal is sectioned into 24 active elements which are electrically isolated from each other by scoring the signal lead side with a high speed diamond

saw. Consequently, each detector element has a width of 2 mm and a height of 10 mm. Using these dimensions and an x-ray tube with with a small (less than 1 mm) focal spot, a resolving power of better than 2 mm can be expected (12). This spatial resolution is adequate for bone mineral determination in the spine. A scale drawing of the germanium crystal indicating the surface scoring technique is given in figure 6.

There is a potential disadvantage to the use of high-purity germanium. The production of germanium crystals of sufficient purity for gamma ray detection is currently very expensive. Impurity concentrations must be kept on the order of 10^{14} atoms cm^{-3} (2 parts per billion) to keep the impurities from significantly affecting the energy resolution of the detector (44). As of 1987, to grow and machine a single crystal of dimensions quoted above of sufficient purity for gamma ray detection costs approximately $6000. Hopefully research into the technology of high-purity crystal growth will reduce this cost in the future.

III. Cryostat Requirements

As explained above, the low value of the band gap energy requires that germanium crystals be operated at liquid nitrogen temperatures to reduce the number of thermally generated electron-hole pairs. But unlike lithium-drifted germanium detectors which may be permanently damaged by warming above 150K, high-purity germanium crystals can be safely cycled to room temperature. A segmented germanium crystal at the UCSF Physics Research Laboratory has been subjected to more

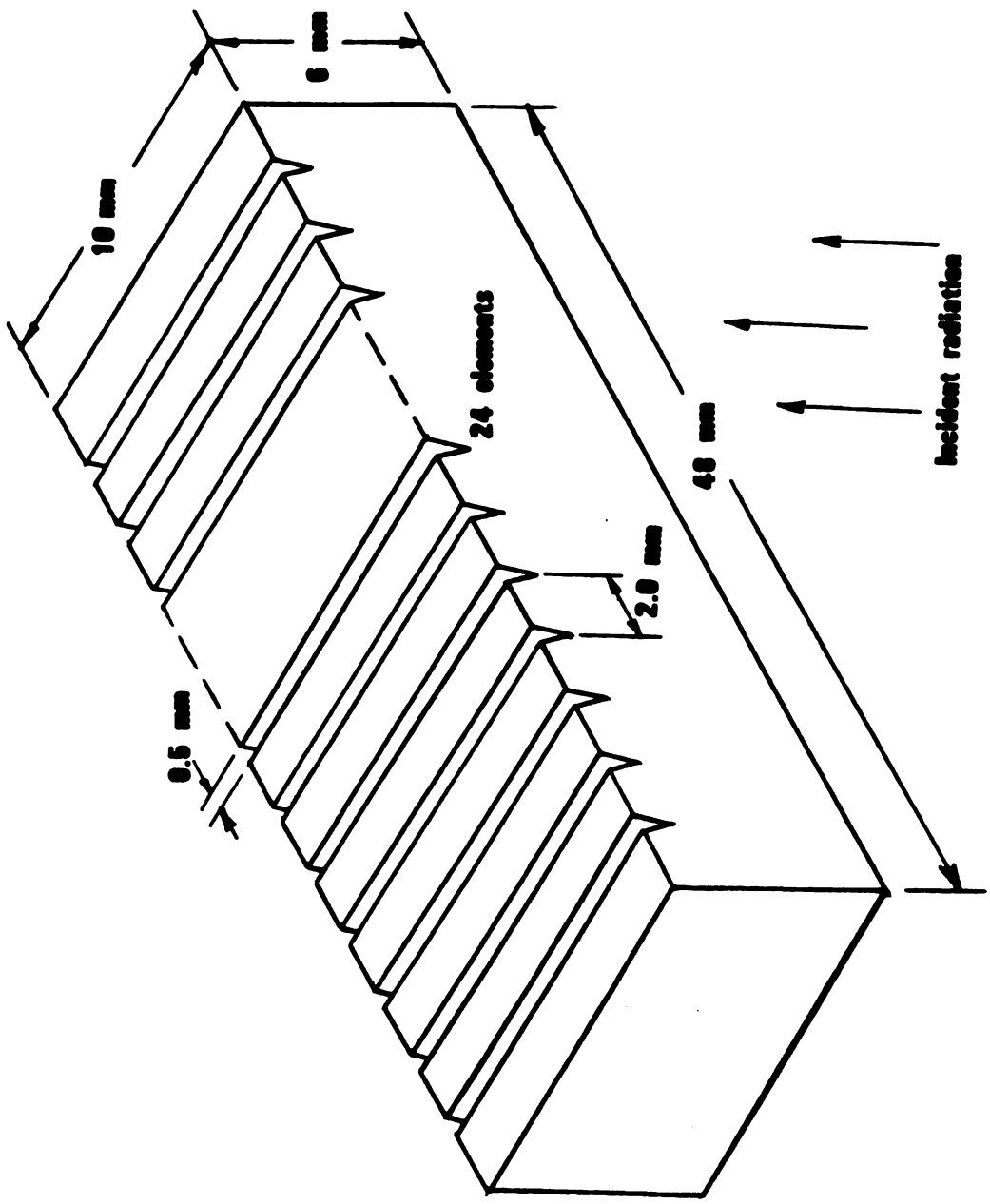

Figure 6: High-purity germanium detector as used in the CTD. A precision diamond saw sections the crystal into 24 active elements. The incident radiation enters the nonsegmented side and creates charge carriers in the reverse biased crystal. These carriers are then collected by electrical plates in contact with the segments to give a signal pulse.

than fifty cycles from 77K to room temperature with no measurable degradation in performance.

High-purity germanium crystals are also extremely sensitive to contamination of the detector surface by dust, fingerprints and condensable vapors. These substances increase the background noise level of the detector by generating surface leakage currents when the crystal is biased under high voltage. To guard against surface contamination, the normal approach is to rely on clean encapsulation techniques, such as a vacuum chamber, and to avoid unnecessary handling of the crystal. Enclosing the crystal in a vacuum chamber also serves to thermally isolate it from the surroundings. Care must be taken that when evacuating the detector chamber no vacuum oil or other vapors are left behind that would condense on the crystal surface upon cooling.

A schematic diagram of a commercially available detector arrangement with associated cryostat is shown in figure 7. Integral detector assemblies of this kind containing nonsegmented germanium crystals can be bought commercially. These cryostat assemblies are however, ill suited for the third generation geometry of the CTD since multiple detectors are needed with minimal dead space.

Third generation geometry requires a detector cryostat design that may be mounted on a rotating gantry opposite the rotating x-ray source. Commercial cryostats are much too large for mounting and can only be operated in a single position, which precludes rotation. The major portion of the work for this thesis involves the design and documentation of a unique rotatable cryostat specifically designed to

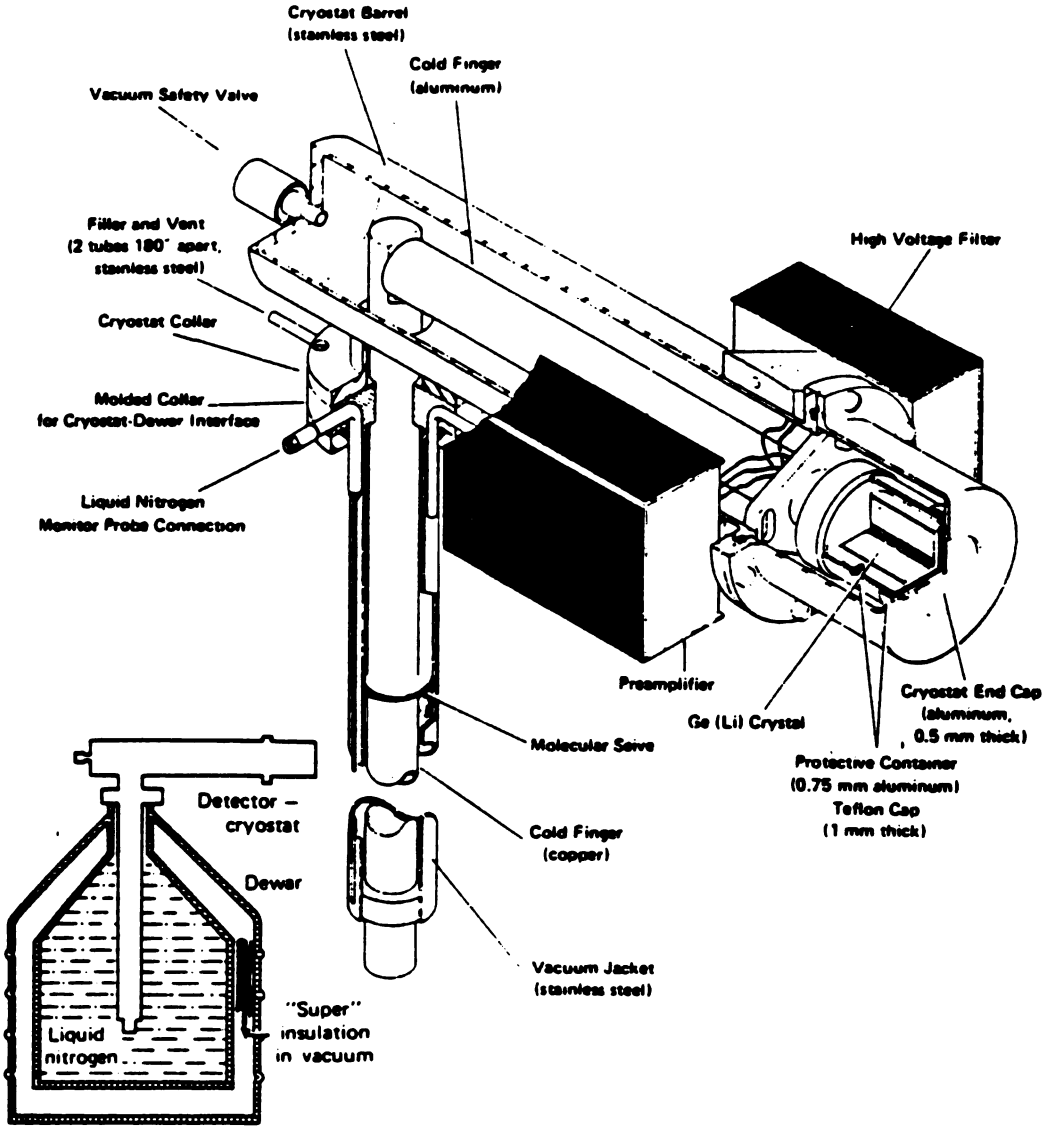

Figure 7: Commercially available cryostat assembly showing the detector crystal attached to the cold finger which is in contact with liquid nitrogen stored in the dewar.

allow for efficient cooling of an array of high-purity germanium detector crystals.

Chapter 3: Design of the CTD Cryostat

Figure 8 shows a sectional view of the assembled CTD Cryostat. Attached to the liquid nitrogen tank are the cold finger and its support which provide the heat transfer path for the cooling of the germanium detectors. The detectors themselves are held in place by the detector mounts secured to the cold finger. Up to nineteen detector mounts may be bolted to the cold finger in an arc as shown in figure 3. Surrounding the entire assembly is a vacuum casing fitted with electrical feedthroughs to the detectors. The detector enclosure is machined with a thin metal window to allow the passage of x-rays to the germanium crystals through the evacuated space. The details in the design of each of the components of the cryostat are present in this chapter.

I. Material

When a solid is cooled, there are three important thermal effects that take place. The first is that the solid itself is cooled; This is described by the heat capacity C_p, which is the energy which must be lost by a single gram of the solid to lower its temperature one degree Kelvin.

The second effect is that the solid transmits the cooling energy. This conduction capability is defined by the thermal conductivity, k, which is a measure of the heat transfer in the solid due to the

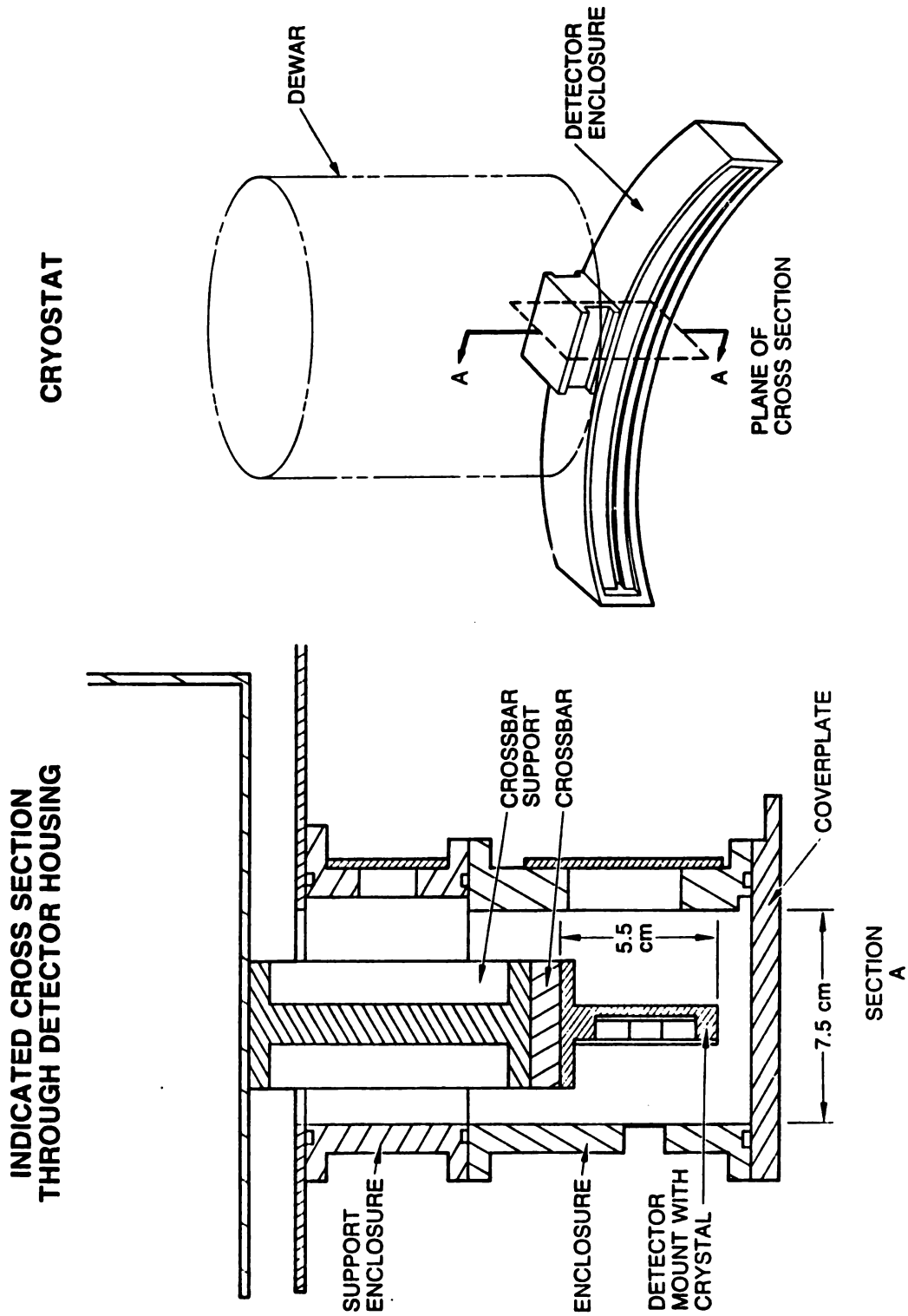

Figure 8: Artist's conception of the assembled CTD cryostat. The cross-section through the tail section shows the detector mount with the germanium crystal, cold finger crossbar, support, and the vacuum enclosure with a thin radiation window.

applied temperature gradient. Thermal conductivity, like the electrical conductivity, is highest for the pure metals and decreases as alloys are added.

The third observed effect is that upon cooling, the solid contracts. A measure of this is the linear coefficient of thermal expansion, $\Delta r/\Delta T$, which expresses the change in length per unit length of the solid (Δr) brought about by a given temperature change (ΔT). Values for C_p, k, and $\Delta r/\Delta T$ for various materials can be found in table 2.

Of the three thermal properties of solids, the thermal conductivity is of the greatest concern for the CTD cryostat. The heat capacity becomes negligible once the material has thermally equilibrated, while any minor thermal contraction effects can be estimated and then compensated for if necessary. Of the thermally conductive metals, copper and aluminum are the most abundant and economical. Aluminum, however, has the advantage of being stronger and lighter than copper, as well as easy to machine. It can also be highly polished which is important for vacuum applications, since interior surface scratches act as traps for air impurities. In addition, a highly reflective surface serves to minimize infra-red heat losses.

The low atomic number and density of aluminum make it an excellent choice for the x-ray window of the detector array enclosure. X-ray attenuation increases with increasing atomic number, so any added alloys must have physical properties comparable to aluminum. Thermal conductivity also decreases as alloys are added, so that the aluminum used for the CTD cryostat must be fairly pure. 6061 aluminum is such an alloy, containing only 1.0% magnesium and 0.6% silicon and exhibiting excellent tensile and thermal properties. The

Table 2. Thermal Properties of Various Materials at 300K

M = Atomic mass

C_p = Specific Heat

$\Delta r/\Delta T$ = Linear Coefficient of Expansion

k = Thermal conductivity

Material	M g/mole	C_p cal/g-K	$\Delta r/\Delta T$ $K^{-1} \times 10^{-6}$	k W/cm-K
Aluminum	27	0.22	24.1	2.37
Copper	63.5	0.092	17.6	4.01
Gold	197	0.031	13.8	3.18
Iron	55.9	0.11	14.0	0.804
Lead	207.2	0.32	28	0.353
Nickel	58.7	0.105	13.3	0.909
Platinum	195.1	0.031	8.8	0.716
Silver	107.9	0.056	19.5	4.29
Tin	118.7	0.54	23.5	0.516
Tungsten	183.9	0.034	3.95	1.73
Stainless Steel		0.14	17.3	0.45
Glass		0.2	7.2	0.78

From R. M. Rose, L. A. Shepard and J. Wulff, *The Structure and Properties of Materials*, Vol. 4. John Wiley & Sons, Inc., New York (1966)

entire CTD cryostat, including the liquid nitrogen dewar, cold finger, detector mount and detector array enclosure is to be constructed using 6061 aluminum.

II. Liquid Nitrogen Dewar

Liquid nitrogen has been traditionally used for cooling germanium crystals because it is readily available and relatively inexpensive. It boils at 77K which is within the acceptable operating range for high-purity germanium detectors. Some sources suggest that germanium crystals may be effectively used up to 180K without sacrificing performance (44).

There are many kinds of insulated containers used for storing cryogenic fluids and they are generally classified according to the type or method of insulation. Some of the more common include vessels insulated with rigid fiber insulation, vacuum insulated vessels and vacuum vessels with multiple radiation shields. Containers in the vacuum insulation category are often referred to as dewars after Sir James Dewar, who first investigated the use of vacuum insulated vessels before the turn of the century.

Vacuum insulation is the logical choice for the CTD, since the detector crystals require an evacuated enclosure to keep them protected from condensable gases when they are cooled. The challenge is to create a single vacuum space to insulate both the liquid nitrogen dewar and the detector array.

The heat transport across a vacuum insulated space is predominantly by radiation with a slight contribution due to gas

conduction. At low pressures (i.e. below 1 torr), any heat transport due to conduction and convection can be considered negligible when compared to the radiation losses. This assumes that any internal support structures between the inner and outer tank are made of poorly conducting plastics or fiberglass which do not contribute to the heat loss of the system. Ray Sarwinski (San Diego, CA), a cryogenics specialist and consulting engineer on the project, has designed just such a support structure using a glass-epoxy composite material (G-10) commonly used for printed circuit boards in a cross-hatched pattern. This structure will serve to support the inner tank to allow rotation, yet it will not significantly increase the thermal conduction across the vacuum gap. By placing the support under tension, the vibration of the internal cryostat structures will be minimized.

A spherically shaped tank is the ideal for cryogenic liquid storage due to the minimal surface to volume ratio, however manufacture of concentric spheres is difficult. A cylindrical tank is much easier to machine and provides an acceptable surface to volume ratio as long as the diameter and height of the tank are kept about equal. As for the heat loss rate, NASA engineers have developed a semi-empirical equation for the heat loss rate of cryogenic tanks valid when the insulated space is adequately evacuated (to 10^{-4} torr) and the inner tank is wrapped with multiple (i.e. 30 to 50) layers of 0.00025 inch aluminized Mylar™ (45). The aluminized Mylar™, more commonly known as "super insulation", serves to greatly reduce the radiation heat transport across the vacuum gap. The formula is

$$dQ/dt = (A/N)\{[10^{-12} \times (T_h^4 - T_c^4)] + [4.2 \times 10^{-8} \times D^{1.5} \times (T_h - T_c)]\} \quad \text{(eqn. 1)}$$

where:

dQ/dt = heat flow in watts

A = area of one of the surfaces in square inches

N = number of Mylar™ layers

T_h = high temperature in Kelvin

T_c = low temperature in Kelvin

D = layer density in sheets per inch

For design purposes, consider two 1 m square aluminum plates, one at 293K, the other at 77K, separated by a 2 cm evacuated space filled with 50 layers of aluminized Mylar™. The surface area A is 1 m^2 or 1550 in^2, and the layer density D is 25 sheets per cm or about 63 sheets per inch. Using these values, dQ/dt is calculated to be 0.368 watts. Allowing for additional conduction losses through the liquid nitrogen fill spout and the internal support structure, a heat loss rate of 0.5 watts is a reasonable estimate for the tank alone.

Besides losses through the dewar tank itself, heat losses can also be expected at the junctions between the tank, cold finger, cold finger support and detector mounts. Tiny air spaces at these junction points will greatly increase the thermal resistance as well as the heat loss rate. Thin sheets (approximately 0.5 mm) of indium metal at each of these junctions can be used to fill any air gaps and decrease the effective thermal resistance at each of these points. With the indium inserts, NASA engineers estimate that a total heat loss of about 1 watt can be

expected in the thermal joints of the system, 0.5 watts along the cold finger itself and 0.5 watts in the support.

Finally, heat conduction paths can be expected along all of the electrical connections passing into and out of the cryostat. This can be somewhat minimized by using stainless steel leads rather than copper (see Table 2). By using Fourier's Law, the loss due to a single lead can be calculated given the dimensions and thermal conductivity of the stainless steel. The heat loss Q can be expressed as:

$$Q = kA\,\Delta T/d \qquad \text{(eqn. 2)}$$

where d is the length of the signal wire, A is the cross-sectional area of the wire, ΔT is the temperature difference across the wire, and k is the thermal conductivity.

For a flex circuit with .002 by .025 inch stainless steel leads 10 cm in length exposed to a temperature difference of (293 - 77) or 216K, the heat loss per lead is calculated as 0.56 milliwatts (mW). For this calculation, a thermal conductivity of 80 mW/cm-K for stainless steel at 80K was used. The cryostat design calls for 24 signal leads plus a single ground lead per module, or a total of 475 leads. Thus the heat loss due to the signal and ground connections is calculated as 266 mW.

In addition to the signal and ground leads, each module requires a high-voltage and test lead which provide yet another heat loss path. These connections will be made using AWG 36 25/50 wire which is composed of 25 woven strands of .001 inch diameter stainless steel. By using equation 2 and performing a similar computation to that above, the heat loss contribution from each 10 cm wire is found to be

5.5 mW. For 19 modules, each with one high-voltage and one test lead, the heat loss is 209 mW. In total, the expected heat loss due to all the electrical connections of the cryostat is on the order of 500 mW or 0.5 watts.

As a first estimate, the total heat loss rate of the cryostat system when all potential heat leak paths are considered should be around 2 watts. Liquid nitrogen can supply 44.8 watt-hours per liter of cooling power to the system, so that 2/44.8 or .045 liters of liquid nitrogen will boil off per hour, which is approximately 1 liter per day. A 5 liter capacity will allow the detector array to be cooled down at the beginning of the week and then remain operational until the weekend.

Since the tank is to be mounted on its side to allow rotation, a 10 liter tank will be needed to hold 5 liters of liquid nitrogen without allowing any to leak out of the fill spout. Assuming a one to one aspect ratio, the inner cylindrical tank will have interior height and diameter dimensions of 24 cm. Allowing for a 2 cm insulation space around the tank and another 2 cm for the total thickness of the inner and outer tank walls, the entire dewar will be under 30 cm in height and diameter.

III. Cold Finger and Support

The cold finger and its support provide the intermediate heat conduction path between the liquid nitrogen tank and the detector modules. Together they must be able to conduct the thermal energy of the germanium crystals away from the detector mounts and to the liquid nitrogen dewar where it can be dissipated. To do this

effectively, the cold finger and support must both have sufficient cross-sectional area to minimize the temperature gradient along their length. The greater the cross section of the heat path, the less is the thermal resistance.

A temperature drop equal to or less than 2K along the length of the cold finger will insure a maximum 0.25 percent variation in the temperature of the detector crystals. Thus any thermally generated leakage currents will be consistent along the detector array. Since each of the 19 crystals is 48 mm long, the total length of the mounting cold finger is 19 x 48 or 912 mm. Only half of this length, however, is involved in the heat conduction path since the support is attached to the middle of the cold finger.

Using a thermal conductivity for aluminum at 80K of 2.3 W/cm-K and estimating the heat leak to be 0.5 watts (as was assumed in the design of the dewar), equation 2 can be solved for the minimum cross-sectional area of the cold bar:

$$A_{min} = Qd/k\Delta T_{max} \qquad \text{(eqn. 3)}$$

Inserting the values into the above equation yields a minimum area of 4.96 cm^2. A 5 by 1 cm cross-section for the cold finger gives the necessary heat transport while providing an adequate flat surface for the mounting of the detector crystal mounts.

The dimensions of the cold finger support can be calculated in a similar fashion as above, allowing for the shorter length. The support is designed to be 10 cm long, allowing for an offset of the detector array from the liquid nitrogen tank. This space is to keep the tank from

interfering with either the x-ray beam or the patient and also provides a convenient place for feeding through the high-voltage, test pulse and temperature probe leads. The feedthroughs are mounted on the enclosure surrounding the support, and the wires are run through the evacuated space to the detector mounts.

Since the support is much shorter than the cold finger, a temperature gradient of only 1K is a reasonable requirement. Setting d equal to 10 cm and ΔT_{max} to 1K in equation 3 while leaving k and Q as above gives a value for A_{min} of 2.17 cm^2. The proposed support design, however, has a cross-sectional area five times that of A_{min} in order to provide the necessary structural stability. Therefore, the temperature gradient along the support section can be expected to be much less than 1K.

The dimensions and details of the cold finger and its support can be found in drawings 1 and 2 of Appendix B. The placement of the mounting holes for the crystal mounts is extremely critical, since any positioning errors will lead to image reconstruction errors. The radius of curvature of the cold finger and angular positioning of the detector mounting holes were designed to correlate with the distance between the x-ray source and detectors as defined by the Technicare 2010 gantry geometry.

On the recommendation of Ray Sarwinski the critical dimensions of the cold finger were increased by 0.4 percent to compensate for thermal contraction at 80K. Thermal contraction at other points in the cryostat were not accounted for since they will not significantly affect the detector alignment.

To check the temperature of the detector array, three platinum resistors are installed on the cold finger. These act as thermal sensors in that their electrical resistance is a strong function of the temperature. Normally they are calibrated to 100Ω at 273K (0°C); any rise or drop in resistance corresponds to a rise or drop in temperature. A specially calibrated meter provided by the manufacturer converts the resistance value to a temperature reading with an error of only ±1%, so that any temperature rise along the detector array due to a vacuum leak or an empty liquid nitrogen dewar can be readily detected.

IV. Detector Crystal Mount

Individual mounts are required to align and secure each of the 19 germanium detector crystals to the cryostat cold finger. These mounts must allow x-rays to enter the unscored side of the crystal while providing electrical connections to each of the scored channels on the opposite side. The mount must also be able to transmit the 500 volt potential drop across the crystal which is necessary to collect the x-ray generated electron-hole pairs. Finally, the detector crystal mount must serve as the last step in the thermal path from the liquid nitrogen dewar to the crystal itself.

Technical drawing 3 in Appendix B shows the detector mount design for the CTD cryostat. The machined high-purity germanium crystal sits on a printed circuit board fastened to the aluminum mount. The circuit board is etched with 24 traces corresponding to the dimensions of the detector crystal designed to collect the signals from each individual detector channel. Projecting from the back side of the

circuit board and through the detector mount are the signal and ground pins for each of the detector channels. From these pins, the signals collected from the crystal can be fed to the preamplifiers via commercially available connectors and a specially designed flex circuit.

Two aluminum coverplates secure the crystal to the circuit board by applying pressure to the outer edges of the crystal face. By using two coverplates, the majority of the crystal face is left exposed, leaving only the thin detector enclosure window between the x-ray beam and the detectors. The cover plates are electrically insulated from the rest of the detector mount by means of a second circuit board, so that the top side of the crystal may be electrically biased with respect to the scored side. The bias voltage is fed to an insulated standoff on the back side of the mount and then carried via a small wire through holes in both the mount and lower circuit board on to the upper circuit board.

Cooling of the crystal occurs directly through the lower circuit board which is fastened to the aluminum detector mount. At first it was feared that the low thermal conductivity of the circuit board material would be a hindrance to adequate cooling of the crystal. In order to test this theory, a mock-up of the detector mount was machined and then fitted with a section of circuit board. A temperature sensitive platinum resistor was then epoxied to the face of the circuit board using a thermally conductive vacuum resin, and the entire assembly was mounted in a test cryostat.

After filling the dewar with liquid nitrogen, the equilibrium temperature of the circuit board configuration was 79K, the same as the recorded temperature of earlier experiments conducted using a mount without the circuit board. Thus it was concluded that the

cooling through the circuit board has little effect on the equilibrium temperature of the system.

Aptec Engineering (Toronto, Ontario) was responsible for machining the high-purity germanium crystals and securing them to the detector mounts. To date, fourteen crystal/mount assemblies have been received by the Physics Research Laboratory, and the crystals are currently being evaluated to be sure they meet the necessary noise and energy resolution requirements. As for the mounts themselves, no thermal, electrical nor structural problems have been encountered.

V. Detector Array Enclosure

The degree of attenuation of the transmitted beam in the aluminum window of the detector array enclosure depends upon the thickness of the window and can be determined from the equation

$$I = I_o e^{-\mu d} \qquad \text{(eqn. 4)}$$

where I_o represents the incident radiation intensity of a monoenergic beam assuming narrow beam geometry, I is the transmitted intensity, d is the thickness of the aluminum window and μ represents the linear attenuation coefficient for aluminum. It is apparent from equation 4 that an infinitely thin window would cause the least amount of attenuation. However, this is impossible from a structural point of view, since the aluminum window must be able to withstand a roughly one atmosphere pressure gradient as well as be reasonable to machine.

One atmosphere pressure along the window equates to 1.013×10^5 N/m^2 or 0.1013 N/mm^2. Consider a 10 mm high by 1000 mm long window which is 1 mm thick constrained along the edges and subject to this pressure. The force acting on the surface of the window, F_w, is the pressure, P, times the surface area of the window, A_w. The surface area is found to be (1000)(10) mm^2, or 10^4 mm^2 . Therefore,

$$F_w = PA_w \qquad \text{(eqn. 5)}$$
$$= (0.1013 \text{ N/mm}^2)(10^4 \text{ mm}^2)$$
$$= 1013 \text{ N}$$

This force is distributed along the constrained edges of the window, creating in a shearing force, F_S, between the thin window edge and the array enclosure. The total area of the window edge is the sum of the areas of both ends and the upper and lower edges, or 2(1 x 10) + 2(1 x 1000) or 2020 mm^2. The resulting shear force is then found to be

$$F_S = (1013\ N) \div (2020\ mm^2)$$
$$= 0.501\ N/mm^2$$

A materials property table (46) lists the yield strength for annealed 6061 aluminum to be 55 N/mm^2, which is a factor of 100 greater than the estimated shear force on the 1 mm thick window. (The yield strength of a material is defined as the stress at which a plastic deformation of 0.2% occurs.) Therefore, the 1 mm thick window should be sufficiently strong to withstand an atmospheric pressure gradient.

To determine the amount of beam attenuation in the 1 mm window, an accurate value of the attenuation coefficient needed to be determined for both low and high energy x-ray beams for use in equation 4. The incident beams from an x-ray tube are not mono-energetic; what is termed a 120 kVp x-ray beam actually is composed of x-rays with energies ranging up to 120 keV. Thus the desired value of the integrated attenuation coefficient is best determined experimentally or through computer simulation techniques.

At the Physics Research Lab, the attenuation coefficient was experimentally determined by placing a series of 1 mm aluminum

plates in 60 and 120 kVp x-ray beams and measuring the transmitted signal (I) using a sodium iodide scintillating crystal. The incident radiation intensity (I_o) was recorded as the signal intensity without any plates in the beam path.

Using semi-logarithmic paper, the ratio I/I_o was plotted as a function of the aluminum thickness d for 60 and 120 kVp x-ray beams. The slope of the lines drawn through the data points gives the attenuation coefficient for aluminum at each energy. From these plots, μ for the 60 kVp beam was determined to be 1.93 cm^{-1} and for the 120 kVp beam to be 0.97 cm^{-1}.

Using a value of 1 mm (= 0.1 cm) in equation 4 along with the experimentally determined values for μ:

$$I/I_o \text{ (at 60 kVp)} = e^{-(1.93)(0.1)} = 0.824 \text{ or } 82.4\%$$
$$I/I_o \text{ (at 120 kVp)} = e^{-(0.97)(0.1)} = 0.908 \text{ or } 90.8\%$$

For the 1 mm window,the majority of the x-ray beam is transmitted through the aluminum with a slight beam hardening effect do to the greater attenuation of the low energy beam. Given these considerations for strength and attenuation, a thickness of 1 mm was chosen, mostly due to the difficulty in accurately milling a curved aluminum window much thinner than this. The window design, as well as the specific dimensions of the detector array enclosure, are shown in drawings 4 and 5 of Appendix B.

All the electrical connections into and out of the enclosure are accomplished via commercially available hermetically sealed feedthroughs soldered onto brass mounting plates. The mounting

plates, which are pictured in drawing 6 in Appendix B, are then secured to the enclosure using screws and standard o-ring seals. The plates are made of brass to insure a good solder joint between the connector and the mounting plate, since aluminum solder joints are not generally considered to be reliable under vacuum conditions. By placing the connectors for each detector crystal on separate mounting plates, every detector module is provided with a convenient side access panel in addition to the bottom coverplate access seal.

It is also important that the preamplifiers of the data acquisition system be placed as close to the detectors as possible to avoid unnecessary losses of the signals before they can be recorded. The screw holes in the top of the array enclosure provide a place for mounting the preamplification circuit boards and are designed to plug directly into the sealed feedthroughs. A curved card cage designed by consulting engineer Suresh Mehta (Pleasanton, CA) will fit onto the mounting holes and support the preamp boards during rotation. By Modifying the existing cable wind-up system of the Technicare gantry, the signal cables from the preamplification circuits will be fed into the energy discriminating electronics of the CTD system which are mounted on a rack adjacent to the CTD gantry.

Also incorporated into the detector array enclosure is a hinge system conceived by Dr. Bruce Hasegawa of the Physics Research Lab and used to mount the entire assembled detector cryostat to the gantry. The two components of the hinge are shown on drawing 7 in Appendix B. The hinges allow access to the detector array by exposing the bottom coverplate. Guide pins on the gantry and corresponding

holes in the enclosure insure realignment of the cryostat after it has been moved.

VI. Conclusions

A test cryostat of similar configuration made from 6061 aluminum is currently in use at the Physics Research Laboratory for the initial testing of the germanium crystals. This test cryostat differs from the final version only in the liquid nitrogen tank capacity and the detector geometry. Instead of an arc of 19 detectors, the test cryostat holds only 3 detector modules on a simplified straight cold finger. This cryostat with three germanium crystals has been successfully used to perform dual photon absorptiometry studies using a samarium filtered x-ray beam.

The liquid nitrogen consumption of the prototype is roughly one liter per day which agrees with the predicted value. Using temperature sensitive resistors, the detector module temperature at the end of the shortened cold finger was verified to be 83K. So far, all the electrical connections and vacuum seals have performed well in this test cryostat.

Some discussion has been raised as to the possibility of replacing the liquid nitrogen dewar with a refrigeration unit. This would eliminate the need for weekly fillings at the expense of portability. For an earth based unit this idea is attractive, however this idea becomes impractical in a device designed for space travel. It also apparently precludes rotation of the cryostat on the gantry, but this problem can be solved by using a wind-up system for the refrigerator hoses.

Conversion between a refrigerated cryostat and liquid nitrogen cryostat should be possible by simply altering the cold finger to accommodate a refrigerator instead of a dewar. The first CTD will likely use a refrigerator for convenience in testing and evaluation of measuring capabilities of the system.

At the time of writing, the CTD cryostat is being machined according to the dimensions presented above. Assembly of the entire CTD including the gantry, cryostat, x-ray tube, patient table, associated electronics and computer system is now proceeding. The cryostat will initially be assembled with only 15 detector crystals (360 total elements) with the option to expand to 19 crystals by adding two detector modules to each end of the cold finger. Delivery of the CTD system to NASA is planned for the middle of 1988.

Appendix A: Bone Mineral Techniques

A) Radiogrammetry

Radiogrammetry involves taking a radiograph of a peripheral site (typically the metacarpal shafts) and measuring the cortical thickness using a caliper. Unusually thin cortices or abnormal changes in cortical thickness from previous studies suggest excessive resorption and loss of skeletal integrity. This method, though easily performed, turns out to be relatively insensitive to small mineral changes since only cortical bone resorption is reflected. In addition, the correlation between the cortical thickness of peripheral bones and the strength of the weight bearing bones of the body is unreliable (47).

B) Single Photon Absorptiometry

Single photon absorptiometry uses an iodine-125 source and a sodium iodide scintillation detector to measure the mineral content of the radial shaft. The measurement is primarily an indication of cortical bone mineralization, since the diaphysis, where measurements are generally made, contains little trabecular bone. The metaphysis, which contains proportionally more trabecular bone (up to 10 to 25 percent of the total bone), is more difficult to measure due to repositioning errors (48). Clinically, this method has proven to be reproducible and fairly accurate, but as with radiogrammetry, single photon

absorptiometry is relatively insensitive to small changes in bone mineral content. The turnover rate of trabecular bone has been reported to be eight times that of cortical bone (13). This suggests that any bone mineral techniques that measure primarily cortical bone will be at the best only one-eighth as sensitive to small mineral content changes as methods which are capable of measuring trabecular bone.

C) Neutron Activation Analysis

Due to the limitations of cortical bone studies, several methods have been developed which measure the mineral content of integral bone, which, in the spine, is a summation of cortical and trabecular bone. In neutron activation analysis, a beam of 1 to 15 MeV neutrons from an accelerator or radioactive source interacts with a portion of the calcium-48 of the body to produce radioactive calcium-49 (half-life of 8.7 minutes) which is counted externally as it decays. Since calcium comprises a constant fraction (0.395) of the skeletal bone mineral, an estimate of mineral content can be made. Radiation doses for such measurements range from 200 to 3000 mrem, depending on the neutron energy and the detector efficiency.

D) Dual Photon Absorptiometry

Bone mineral measurement accuracy for single photon absorptiometry is known to be degraded by variable fat or marrow content. One solution to this inaccuracy is the use of two photon energies which allows the influence of variable fat content to be

eliminated. In dual photon absorptiometry, two photons of different energies are used to make transmission measurements at several points of the body. Typically, a high activity gadolinium-153 source is used, providing a stable source of 42 and 100 keV photons which are counted by a sodium iodide scintillation detector. Differences in the attenuation of the two photon energies provide the means to estimate skeletal bone mineral content. The dual energy technique has also proven to be an excellent way to distinguish between different body tissues, since attenuation coefficients are strongly energy dependent. A typical scan requires anywhere from twenty to forty minutes, though new developments using an x-ray tube and multiple detectors should reduce the time to around five minutes. As with neutron activation analysis, however, only integral bone is measured, which limits sensitivity due to the inclusion of cortical bone.

Appendix B: Technical Drawings

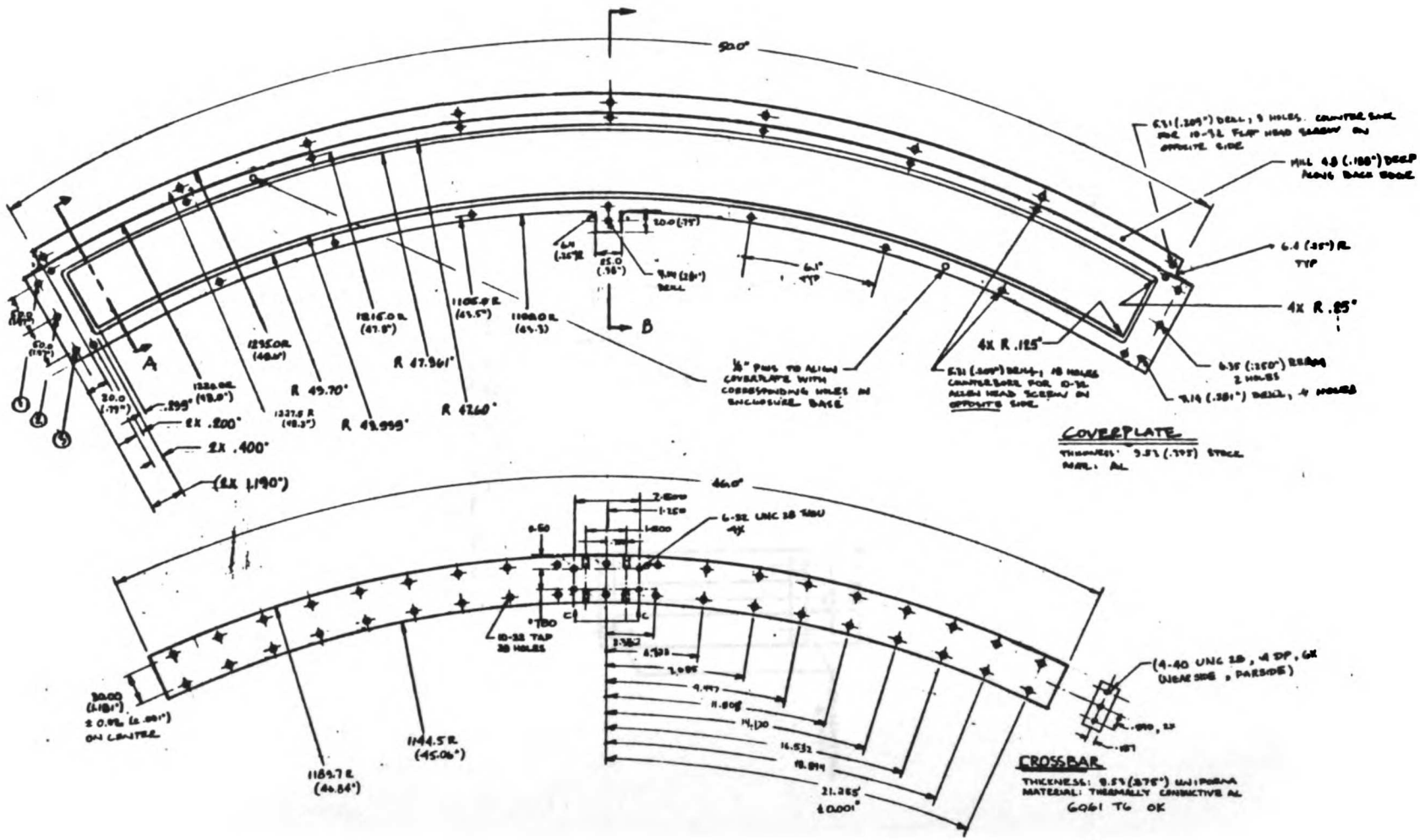
52.0°
6.31 (.249") DEEP; 9 HOLES. COUNTERSINK FOR 10-32 FLAT HEAD SCREW ON OPPOSITE SIDE
MILL 4.8 (.190") DEEP ALONG BACK EDGE
6.4 (.25") R TYP
4X R .85"
4X R .125"
6.35 (.250") DEEP 2 HOLES
9.14 (.361") DEEP; 4 HOLES
½" PINS TO ALIGN COVERPLATE WITH CORRESPONDING HOLES IN ENCLOSURE BASE
6.31 (.249") DEEP; 18 HOLES COUNTERBORE FOR 0-32 ALLEN HEAD SCREW ON OPPOSITE SIDE
COVERPLATE
THICKNESS: 9.53 (.375") STOCK
MAT'L: AL
46.0°
6-32 UNC 2B THRU
10-32 TAP 20 HOLES
(4-40 UNC 2B, .4 DP, 6X (NEAR SIDE, PARSIDE)
CROSSBAR
THICKNESS: 9.53 (.375") UNIFORM
MATERIAL: THERMALLY CONDUCTIVE AL 6061 T6 OK

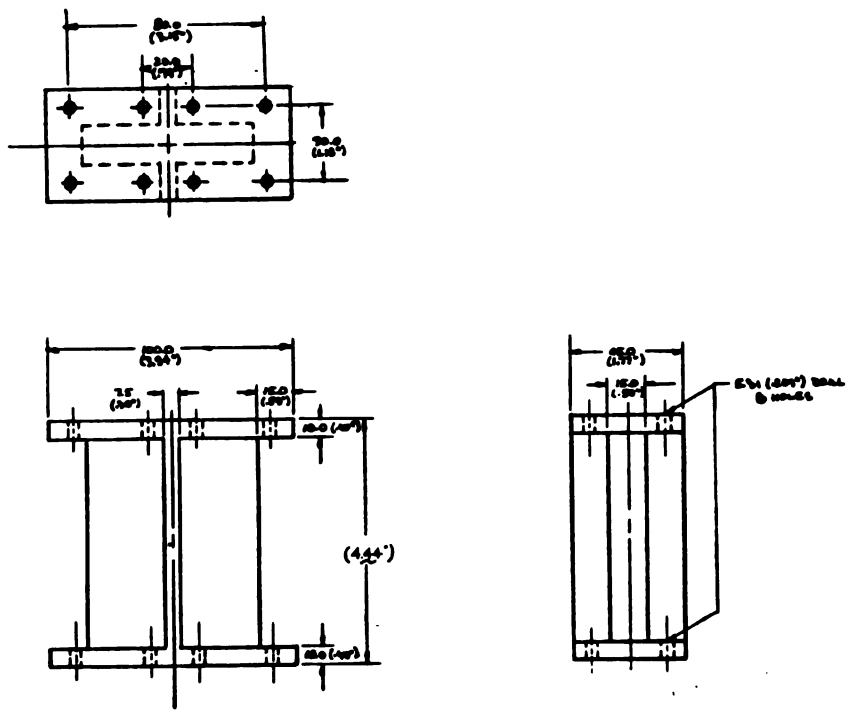

CROSS BAR SUPPORT

MATERIAL: THERMALLY CONDUCTIVE AL

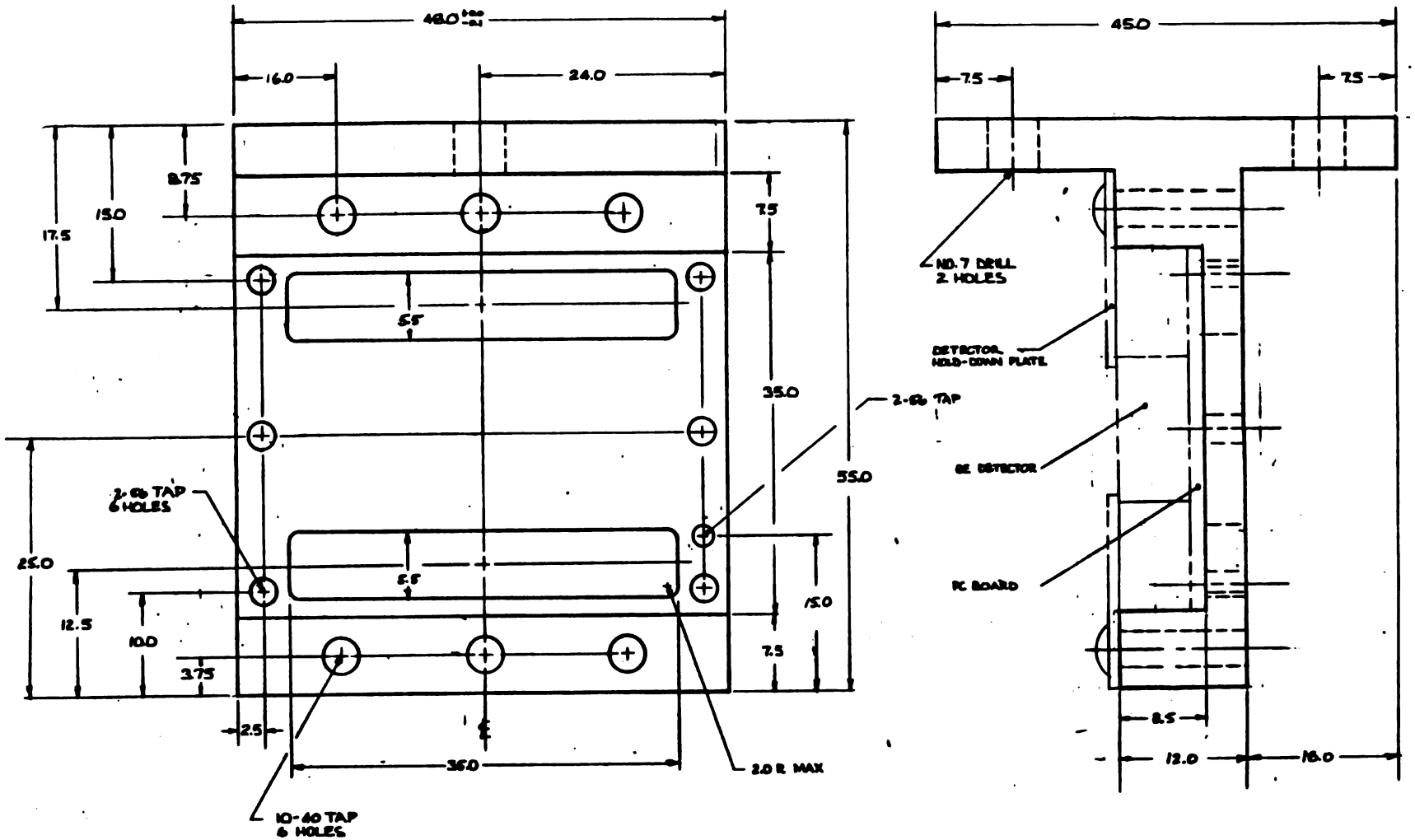
48.0 +.00 -.01
16.0
24.0
8.75
15.0
17.5
7.5
5.5
35.0
55.0
2-6b TAP
2-6b TAP
6 HOLES
25.0
5.5
15.0
12.5
10.0
3.75
7.5
2.5
36.0
2.0 R MAX
10-40 TAP
6 HOLES
45.0
7.5
7.5
NO. 7 DRILL
2 HOLES
DETECTOR
HOLD-DOWN PLATE
6E DETECTOR
PC BOARD
8.5
12.0
18.0

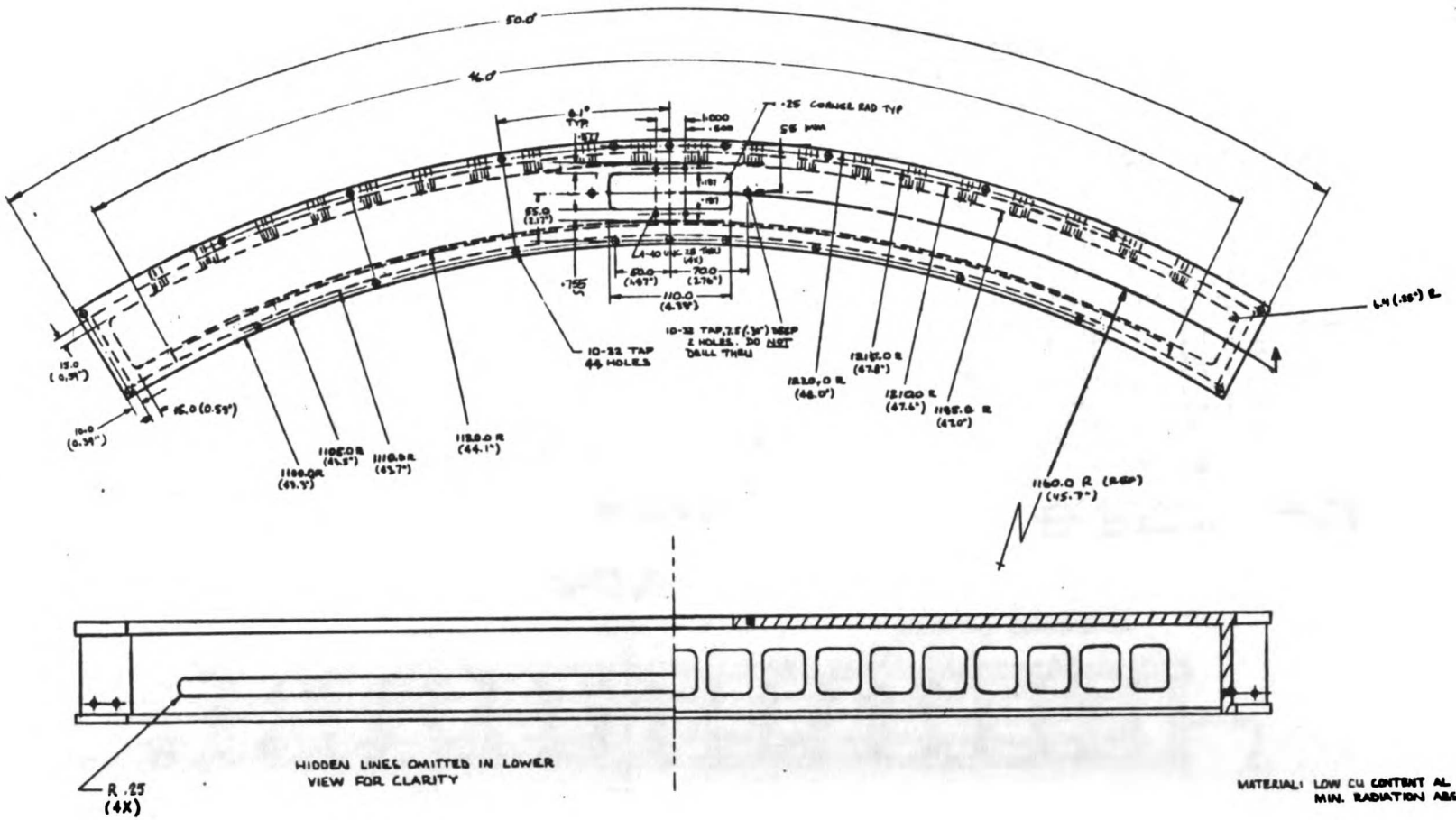
50.0
46.0
.25 CORNER RAD TYP
55 MIN
10-32 TAP
44 HOLES
10-32 TAP, 2.5 (.98") DEEP
2 HOLES. DO NOT
DRILL THRU
4-40 UNC-2B THRU
(4X)
110.0
(4.33")
60.0
(1.97")
70.0
(2.76")
55.0
(2.17")
15.0
(0.59")
10.0
(0.39")
16.0 (0.63")
1160.0 R
(45.7")
1160.0 R (REF)
(45.7")
1138.0 R
(44.8")
1138.0 R
(44.1")
1160.0 R
(45.7")
1160.0 R
(45.7")
1160.0 R
(45.7")
1160.0 R
(45.7")
1160.0 R
(45.7")
R .25
(4X)
HIDDEN LINES OMITTED IN LOWER
VIEW FOR CLARITY
MATERIAL: LOW Cu CONTENT AL. FOR
MIN. RADIATION ABSORBTION

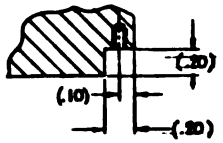

DETAIL "B"
SCALE : NONE

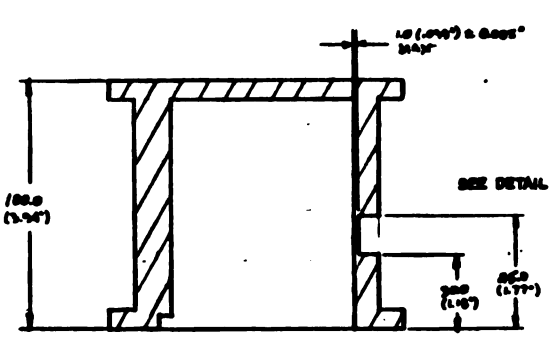

SECTION A
FULL SCALE

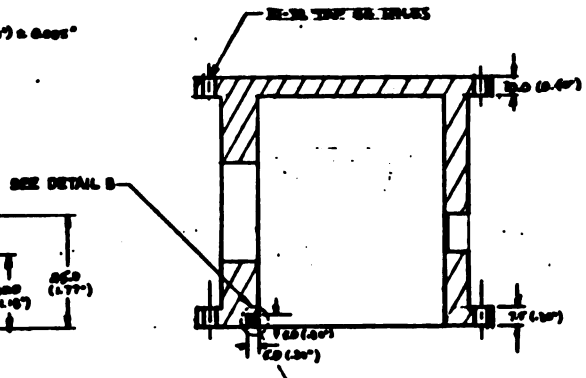

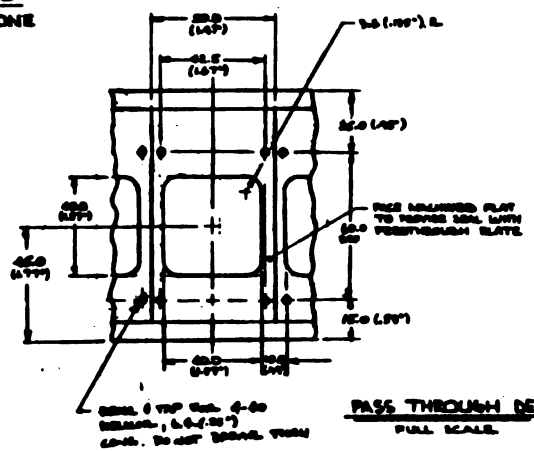

PASS THROUGH DETAIL
FULL SCALE

SECTION B
FULL SCALE

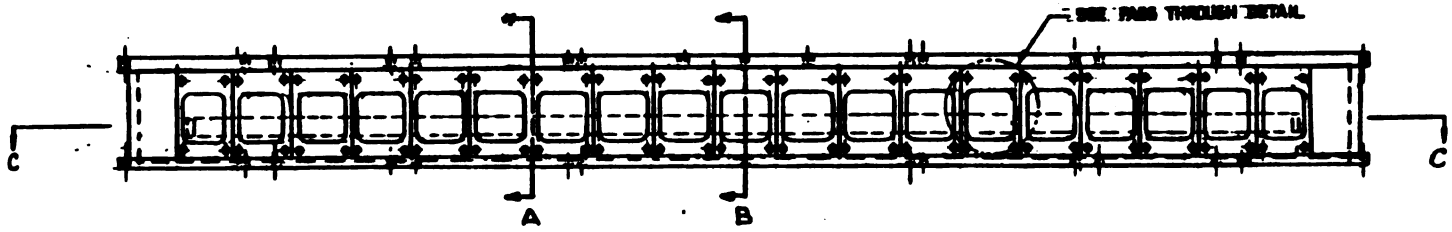

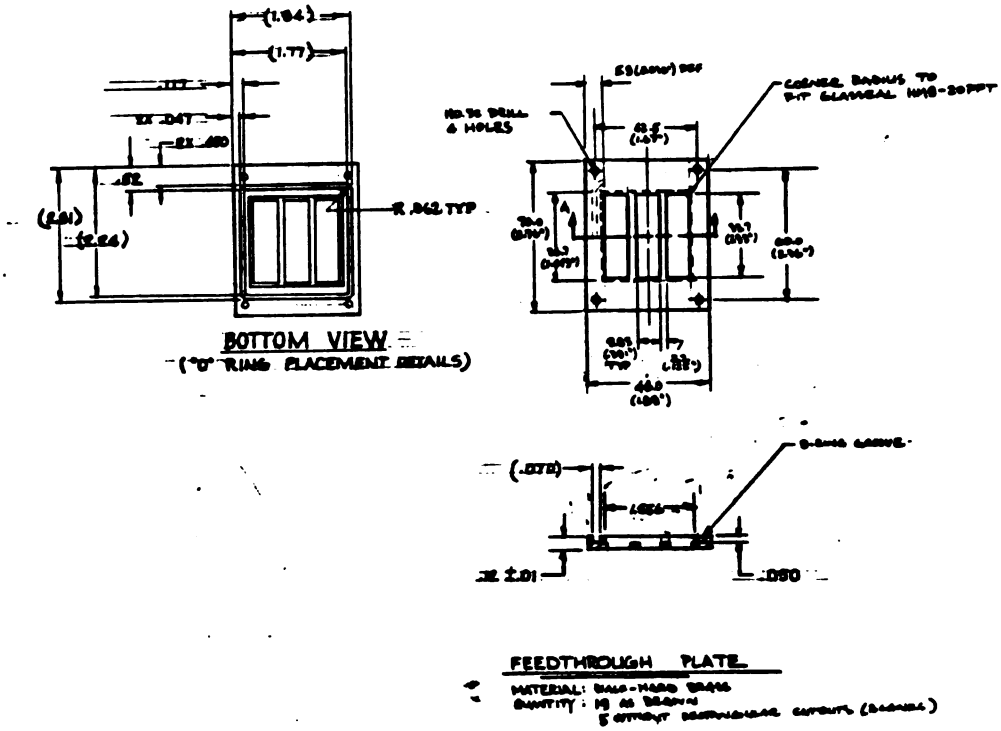
(1.84)
(1.77)
2X .047
2X .080
.82
(2.81)
(2.86)
R .062 TYP
BOTTOM VIEW
("O" RING PLACEMENT DETAILS)
CORNER RADIUS TYP
FOR STANDARD MIL-38999
(.057)
.050
FEEDTHROUGH PLATE
MATERIAL:
QUANTITY:

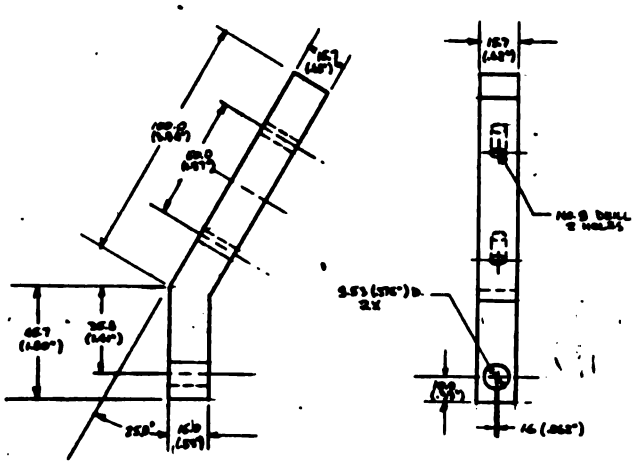

HASEGAWA HINGE (PART 1)

MATERIAL: 3075 Al.
QUANTITY: 2

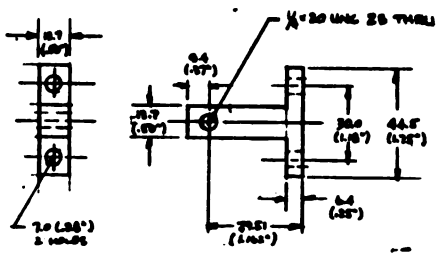

HASEGAWA HINGE (PART 2)

MATERIAL: 3075 Al.
QUANTITY: 2

References

1. Lang SM, Moyle DD, Berg EW, DeTorie N, Gilpin AL, Pappas J, Reynolds JC, Tkacik M, Waldron II RL: Estimation of trabecular bone mechanical properties by CAT. (In) *Transactions of the 33rd Annual Meeting of the Orthopaedic Research Society* 12:51 (1986).

2. Hvid I, Bentzen SM, Jørgensen J: Axial compressive strength of trabecular bone at the proximal tibia assessed by quantitative computed tomography. (In) *Transactions of the 33rd Annual Meeting of the Orthopaedic Research Society* 12:52 (1986).

3. Dickie DL, Goldstein SA, Flynn MJ, Ge ZF, Kleerekoper M, Matthews LS: Regional vertebral bone density distribution measurements and their correlation to whole bone strength. (In) *Transactions of the 33rd Annual Meeting of the Orthopaedic Research Society* 12:261 (1986).

4. Struhl S, Goldstein SA, Dickie DL, Flynn MJ, Matthews LS: The distribution of mechanical properties of trabecular bone within vertebral bodies and iliac crests: correlation with computed tomography density. (In) *Transactions of the 33rd Annual Meeting of the Orthopaedic Research Society* 12:262 (1986).

5. Katz I, Pritzker KPH, Grynpas MD: Qualitative bone mineral changes in osteoporosis. (In) *Transactions of the 33rd Annual Meeting of the Orthopaedic Research Society* 12:263 (1986).

6. Kleeman BC, Edwards WT, Hayes WC, Zamenhof RG, Sarno RC, Nachemson AL, White III AA: Prediction of vertebral fracture risk using quantitative computed tomography in vivo. (In) *Transactions of the 33rd Annual Meeting of the Orthopaedic Research Society* 12:264 (1986).

7. Cohen SH, Aloria JE, Letteri JM: *Calcified Tissue Research* 26:1-3 (1978).

8. Mack PB, LaChaure PA, Vose GP, Vogt FB: Bone demineralization of foot and hand of Gemini-Titan IV, V and VII astronauts during orbital flight. *AJR* 100:503-511 (1967).

9. Vogel JM: HEW International Conference on Bone Mineral Measurement, 353-361 (1974).

10. Kransnylch IG: (In) *Nevesemost: Mediko-Bioloicheskije Issledonvaniye*, (Moscow, Meditsina Press, 186-192, 1974).

11. Whedon GD, Lutwak L, Rambaud PC, Whittle MC, Smith MC, Reid J, Leach C, Stadler CR, Sanford DD: Mineral and nitrogen metabolic studies: Experiment M071. (In) Johnston RS and Dietlein LF (eds).

Biomedical Results from Skylab, NASA SP-377, (Washington DC, 1977).

12. Rutt BK, Stebler BG, Cann CE, Boyd DP, Genant HK: A whole body CT scanner for ultra-precise, ultra-accurate determination of bone density. (In) *Proceedings of the 4th International Workshop on Bone and Soft Tissue Densitometry Using CT*, Fontevraud, France (1984).

13. Orphanoudakis SC, Jensen PS, Rauschkolb EN, Lang R, Rasmussen H: Bone mineral analysis using single energy computed tomography. *Invest Radiol* 14:122-130 (1979).

14. Abols Y, Genant HK, Rosenfeld D, Boyd DP, Ettinger B, Gordan GS: Spinal bone mineral determination using computerized tomography in patients, controls and phantoms. (In) Mazess RB (eds). *Proceedings of the 4th International Conference on Bone Measurement*, NIH Publ. 80-1928 (Washington DC, US Government Printing Office) pp 297-308 (1980).

15. Adams JE, Pullan BR, Adams PH, et al: Dual-energy computed tomography (CT) and the estimation of bone mass. (Abst) *J Comput Assist Tomogr* 6:204 (1982).

16. Bradley JG, Huang HK, Ledley RS: Evaluation of calcium concentration in bones from CT scans. *Radiology* 128:103-107 (1978).

17. Cann CE, Genant HK: Precise measurement of vertebral mineral content using computed tomography. *J Comput Assist Tomogr* 4:493-500 (1980).

18. Cann CE, Genant HK, Ettinger B, Gordan GS: Spinal mineral loss in oopherectomized women. *JAMA* 244:2056-2059 (1980).

19. Cann CE, Genant HK: Cross-sectional studies of vertebral mineral content. Proceedings of the Second International Workshop on Bone and Soft Tissue Densitometry Using Computed Tomography. *J Comput Assist Tomogr* 6:216-217 (1982).

20. Cann CE: Low-dose CT scanning for quantitative spinal mineral analysis. *Radiology* 140:813-815 (1981).

21. Cann CE, Genant HK: Single- versus dual-energy CT for vertebral mineral quantification. Proceedings of the 3rd International Workshop on Bone and Soft Tissue Densitometry Using Computed Tomography. *J Comput Assist Tomogr* 7:551-552 (1983).

22. Faul DD, Couch JL, Cann CE, Boyd DP, Genant HK: Composition-selective reconstruction for mineral content in the axial and appendicular skeleton. Second International Workshop on Bone and Soft Tissue Densitometry Using Computed Tomography. *J Comput Assis Tomogr* 6:202-204 (1982).

23. Exner GH, Prader A, Elsasser U, Anliker M: Effects of high dose estrogen and testosterone treatment in adolescents upon trabecular and compact bone measured by ^{125}I computed tomography: A preliminary study. *Acta Endocrinol* 94:126-131 (1980).

24. Genant HK, Boyd DP: Quantitative bone mineral analysis using dual-energy computed tomography. *Invest Radiol* 12:545-551 (1977).

25. Genant HK, Boyd DP, Rosenfeld D, Abols Y, Cann CE: Quantitative bone mineral analysis using computed tomography. (In) Stanley H. Cohn (ed.) *Noninvasive Measurements of Bone Mass and Their Clinical Applications*, (CRC Press, Inc, New York NY, 1981) pp. 121-149.

26. Genant HK, Cann CE: Vertebral mineral determinations using quantitative computed tomography. (In) Deluca HF, Frost HM, Jee WS, Johnston CC, Parfitt AM (eds). *Osteoporosis: Recent Advances in Pathogenesis and Treatment*, (University Park Press, Baltimore MD, 1981) pp. 37-47.

27. Genant HK, Cann CE, Ettinger B, Gordon GS: Determination of bone mineral loss in the axial and appendicular skeleton of oophorectomized women. Proceedings of the Second International Workshop on Bone and Soft Tissue Densitometry Using Computed Tomography. *J Comput Assist Tomogr* 6:217-218 (1982).

28. Genant HK, Cann CE, Ettinger B, Gordon GS: Quantitative computed tomography of vertebral spongiosa: A sensitive method for

detecting early bone loss after oophorectomy. *Ann Int Med* 97:699-705 (1982).

29. Genant HK, Cann CE, Pozzi-Mucelli RS, Kanter AS: Vertebral mineral determinaton by quantitative CT: Clinical feasibility and normative data. Proceedings of the Third International Workshop on Bone and Soft Tissue Densitometry Using Computed Tomography. *J Comput Assist Tomogr* 7:554 (1983).

30. Posner I, Griffiths HJ: Comparison of CT scanning wiht photon absorptiometric measurement of bone mineral content in the appendicular skeleton. *Invest Radiol* 12:524-544 (1977).

31. Pullan BR, Roberts TE: Bone mineral measurement using an EMI scanner and standard methods: a comparative study. *Brit J Radiol* 51:24-28 (1978).

32. Reich NE, Seidelman FE, Tubbs T, MacIntyre WJ, Meaney TF, Alfidi RJ, Pepe RG: Determination of bone mineral content using CT scanning. *AJR* 127:593 (1976).

33. Revak CS: Mineral content of cortical bone measured by computed tomography. *J Comput Assist Tomogr* 4:342-351 (1980).

34. Rüegsegger P, Elsasser U, Anliker M, et al: Quantification of bone mineralization using computed tomography. *Radiology* 121:93-97 (1976).

35. Rüegsegger P, Anliker M, Dambacher M: Quantification of trabecular bone with low-dose computed tomography. *J Comput Assist Tomogr* 5:384-390 (1981).

36. Schneider VS, Hinderling T, Vogel JM, Rambaud R: CT ^{125}I gamma-ray densitometry (CT scanner): Noninvasive measurement of trabecular bone mineral. *J Comput Assist Tomogr* 3:847-848 (1979).

37. Hangartner TN, Overton TR: Quantitative measurement of bone density using gamma-ray computed tomography. *J Comput Assist Tomogr* 6:1156 (1982).

38. Weissberger MA, Zamenhof RG, Aronow S, Neer RM: Computed tomography for the measurement of bone mineral in the human spine. *J Comput Assist Tomogr* 2:253-262 (1978).

39. Stebler BG: Bestimmung der Knochendichte und ihrer graduellen Veränderungen in Extremtäten des Menschen mittels quantitativer Computertomographie, Dissertation ETH 7219, (1983).

40. Goldberg HI, Cann CE, Moss AA, Ohto M, Brito A, Federle M: Noninvasive quantitation of liver iron in dogs with hemochromatosis using dual-energy CT scanning. *Invest Radiol* 17:375-380 (1982).

41. Marshall WH, Easter W, Zatz LM: Analysis of the dense lesion by computed tomography with dual kVp scans. *Radiology* 124:87-89 (1977).

42. Adams JE, Chen SZ, Adams PH, Isherwood I: Measurement of trabecular bone mineral by dual energy computed tomography. *J Comput Assist Tomogr* 6:601-607 (1982).

43. Boyd, DP, Cann CE, Genant HK, Gould RG, and Kaufman L: A proposed multisource CT scanner for ultraaccurate tomodensitometry throughout the body. (In) Proceedings of CT Densitometry Workshop, *J Comput Assist Tomogr* 3:856 (1979).

44. Knoll GF: *Radiation Detection and Measurement*, John Wiley and Sons (1979).

45. Sarwinski, R: Personal communication.

46. Rose RM, Shepard, LA, Wulff, J: *The Structure and Properties of Materials*, Vol. 4. John Wiley & Sons, Inc., New York (1966).

47. Garn SM: The earlier gain and later loss of cortical bone. (In) *Nutritional Perspective* (Springfield, IL, CC Thomas, 1970), pp 146.

48. Wahner HW, Riggs BL, Beabout JW: Diagnosis of osteoporosis: usefulness of photon absortiometry at the radius. *J Comput Assist Tomogr* 6:1156 (1982).